

University of New Hampshire
University of New Hampshire Scholars' Repository

Doctoral Dissertations

Student Scholarship

Winter 2005

Applications of fluorescence detected sedimentation I Studying the thermodynamic impact of valence in non-ideal solutions II High affinity interactions and biological media

Rachel R. Kroe

University of New Hampshire, Durham

Follow this and additional works at: <https://scholars.unh.edu/dissertation>

Recommended Citation

Kroe, Rachel R., "Applications of fluorescence detected sedimentation I Studying the thermodynamic impact of valence in non-ideal solutions II High affinity interactions and biological media" (2005). *Doctoral Dissertations*. 305.
<https://scholars.unh.edu/dissertation/305>

This Dissertation is brought to you for free and open access by the Student Scholarship at University of New Hampshire Scholars' Repository. It has been accepted for inclusion in Doctoral Dissertations by an authorized administrator of University of New Hampshire Scholars' Repository. For more information, please contact nicole.hentz@unh.edu.

APPLICATIONS OF FLUORESCENCE DETECTED SEDIMENTATION

I: STUDYING THE THERMODYNAMIC IMPACT OF VALENCE IN NON-IDEAL
SOLUTIONS

II: HIGH AFFINITY INTERACTIONS AND BIOLOGICAL MEDIA

BY

Rachel R. Kroe

B.S., Chemical Engineering, University of New Hampshire, 1995.

M.S., Biochemistry, University of New Hampshire, 1998.

DISSERTATION

Submitted to the University of New Hampshire
in Partial Fulfillment of
the Requirements for the Degree of

Doctor of Philosophy

In

Biochemistry and Molecular Biology

December, 2005

UMI Number: 3198010

INFORMATION TO USERS

The quality of this reproduction is dependent upon the quality of the copy submitted. Broken or indistinct print, colored or poor quality illustrations and photographs, print bleed-through, substandard margins, and improper alignment can adversely affect reproduction.

In the unlikely event that the author did not send a complete manuscript and there are missing pages, these will be noted. Also, if unauthorized copyright material had to be removed, a note will indicate the deletion.

UMI[®]

UMI Microform 3198010

Copyright 2006 by ProQuest Information and Learning Company.

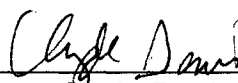
All rights reserved. This microform edition is protected against unauthorized copying under Title 17, United States Code.

ProQuest Information and Learning Company
300 North Zeeb Road
P.O. Box 1346
Ann Arbor, MI 48106-1346

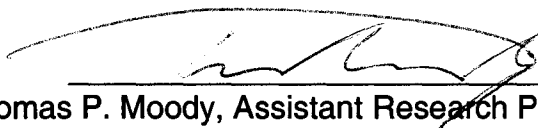
This dissertation has been examined and approved.



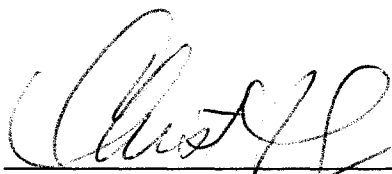
Thesis Director, Thomas M. Laue, Professor




Clyde Denis, Professor



Thomas P. Moody, Assistant Research Professor



Christine A. Grygon, Associate Director
Boehringer Ingelheim Pharmaceuticals



Richard H. Ingraham, Senior Principal Scientist
Boehringer Ingelheim Pharmaceuticals

Nov 7, 2005
Date

ACKNOWLEDGMENTS

B I P H A R M A C E U T I C A L S T Y
C Q M A R T I N I L A N D W U E R J U
D C A B S P A F E B S D S A C P H O I
P T H O M A S L A U E L V I S A G H J
L K A R L A L S E Y D E F G R H E Y J
A K R L I E Z C N A M T R A H I R A K
Y X G C H S H V M B N S W M D I W C
E M N C D A T R L N N B I B V A O E O
R Y I A S C X I 2 N Z N N R A L G G S
T M D E F D S S N A E E E A S A E D T
G N R O S A P S H E K J D D K N R I E
L S A L O U O Y M I G I E L U T G R L
S A H R L M E O N R T R D A R U E Y L
B R C E U I M L W R Q R Y N S T L R O
O A I F A D H O U A H E L G J E L R T
B H R K R O R N T O A T C H O I E E F
E B Y E E 3 B E H G I N D O F N H T D
G E X M V T E H F O P U M R D D C F S
N A S D A B V I R I J G S S K I I P R
O N A B D G M H Y O N U N T G H M L U
P B R E T T A U S T I N E D 2 9 7 K L
S E F L N E H C O R A L E N A I D H E
M A R T H A B A K E R G I J K D O T S

TABLE OF CONTENTS

ACKNOWLEDGEMENTS	iii
LIST OF TABLES	vi
LIST OF FIGURES	vii
ABSTRACT	ix
I. INTRODUCTION	1
II. MATERIALS AND METHODS	6
A. Materials	6
i. Chemicals	6
ii. Commercially Available Macromolecules	6
iii. Expression and Purification of Green Fluorescent Protein	7
iv. Expression and Purification of Barstar	8
v. Recombinant soluble endothelial Protein C receptor (rsEPCR)	9
vi. Antibodies	9
vii. Fluorescently labeled Lipids and Proteins	9
viii. Isolation of Human Serum and Plasma	10
B. Methods	10
i. Sedimentation Velocity (absorbance optics)	10
1. rsEPCR	10
ii. Fluorescence Detection System (FDS) Instrumentation	10
1. Lasers	10
2. Filters	11
3. Photomultiplier Tube (PMT)	11
4. Software	12
iii. FDS Sedimentation Velocity	12
1. FDS of GFP in the presence of varying concentrations of background molecules (Dextran, Soybean trypsin inhibitor and hen egg white Lysozyme)	12
2. FDS of DPPC-NBD in the presence and absence of rsEPCR	14
3. FDS of GFP and anti-GFP	15
4. FDS of Alexa488-BSA and Alexa488-IgG	15
5. FDS of GFP in serum	16
6. FDS of GFP and anti-GFP in serum	16
7. FDS of fluorescein-DPPE in serum	17
8. FDS of GFP in e. Coli lystate	17
iv. Fluorescence Polarization	17
III. GFP AS A PROBE OF NON-IDEALITY IN HIGH CONCENTRATION BACKGROUNDS	19

A. Introduction and Theory	19
B. Results	23
C. Discussion.....	35
IV. APPLICATIONS OF FDS	41
A. Use of FDS to Study Small Molecule-Protein Interactions	44
i. Example1: Studying the interaction between rsEPCR and DPPC/E	44
a. Introduction.....	44
b. Results	46
c. Discussion	48
B. Use of FDS to Study High Affinity Interactions	49
i. Example 2: The interaction between GFP and anti-GFP	49
a. Introduction.....	49
b. Results	49
c. Discussion	52
C. Use of FDS to Study Sedimentation in Physiological Media	54
i. Example 3: Sedimentation Velocity of Alexa488-BSA in Serum and Plasma	54
ii. Example 4: Sedimentation Velocity of Alexa488-IgG in Serum.....	56
iii. Example 5: Sedimentation of GFP in Human Serum	58
iv. Example 6: Sedimentation of GFP-anti-GFP Complex in Serum.....	60
v. Example 7: Sedimentation Velocity of Fluorescein-DPPE in Serum	62
vi. Example 8: Sedimentation of GFP in E. Coli Lysates	63
D. Summary.....	64
REFERENCES.....	66
APPENDIX A: MEASUREMENT OF STOKES RADIUS.....	68
APPENDIX B: FDS OF GFP,IN PEG, OVALBUMIN, RNASE A, HEL AND BARSTAR	71
APPENDIX C: SOLUTION DENSITIES AND PARTIAL SPECIFIC VOLUME OF BACKGROUND MOLECULES	74
APPENDIX D: SOLUTION VISCOSITIES OF BACKGROUND MACROMOLECULES	81
APPENDIX E: ALEXA488-BSA IN VARIOUS HIGH CONCENTRATION BACKGROUNDS	85

LIST OF TABLES

1.	Non-covalent Interactions	39
2.	Apparent sedimentation coefficients, effective reduced molecular weight and the calculated Stokes radius of GFP, Barstar and STI.....	70
3.	Densities and Partial Specific Volumes of Background Molecules	80
4.	Equations for calculating density as a function of background macromolecule concentration	84

LIST OF FIGURES

1.	Predicted effect of excluded volume and charge on the total activity of HEL in high concentrations of HEL	22
2.	The apparent sedimentation of GFP in dilute solution and in a background of 35 mg ml ⁻¹ Dextran	25
3.	The apparent sedimentation coefficient of GFP in Dextran, STI and HEL as function of background molecule	26
4.	Calculated $S_{20,W}$, $D_{20,W}$ and ratio $S_{20,W}/D_{20,W}$ of GFP as a function of Dextran concentration.....	27
5.	The apparent sedimentation of GFP in dilute solution and in 50 mg ml ⁻¹ STI	28
6.	Calculated $S_{20,W}$, $D_{20,W}$ and ratio $S_{20,W}/D_{20,W}$ of GFP as a function of STI concentration	29
7.	The apparent sedimentation of GFP in dilute solution and in 50 mg ml ⁻¹ HEL.....	31
8.	Calculated $S_{20,W}$, $D_{20,W}$ and ratio $S_{20,W}/D_{20,W}$ of GFP as a function of HEL concentration.	32
9.	The activity of GFP as function of Dextran, STI and HEL concentration	33
10.	Ratio of f/f_0 for GFP in Dextran, STI and HEL.....	34
11.	Calculated impact of solution non-ideality on the activity of GFP in Dextran, STI and HEL as compared to experimentally measured values in Dextran, STI and HEL	36
12.	Sedimentation velocity of 14 μ M rsEPCR collected with the absorbance optics and 10 μ M rsEPCR + 400 nM NBD-DPPC collected with the fluorescence optics	47
13.	Sedimentation Velocity of 40 nM GFP titrated with 540 nM, 60 nM, 20 nM, 7 nM and 0.3 nM anti-GFP.....	50
14.	Mass Fraction of 7.8 S and 2.6 S species as a function of antibody concentration	51
15.	Direct binding of GFP to Anti-GFP as measured by fluorescence polarization.....	52
16.	Sedimentation velocity of Alexa488-BSA in buffer Serum and Plasma.....	55
17.	$c(s)$ fit for Alexa488-IgG in buffer and in serum.....	57
18.	Raw sedimentation velocity data for 100 nM GFP in human serum.....	59
19.	Raw sedimentation data of 4 nM GFP in serum and the $c(s)$ fit to the data	60
20.	Raw sedimentation velocity data and $c(s)$ fit for 100 nM GFP + 100 nM anti-GFP in serum.....	61
21.	Raw sedimentation velocity data for 2 μ M fluorescein-DPPE in human serum.....	63
22.	Sedimentation Velocity of 20 nM GFP in buffer and E. Coli Lysate	64
23.	$c(s)$ distribution for 10 nM GFP in buffer, PEG, Ovalbumin and HEL.....	72

24.	Solution density plotted as a function of HEL concentration.....	77
25.	Solution density plotted as a function of STI concentration	77
26.	Solution density plotted as a function of Dextran concentration	78
27.	Solution density plotted as a function of Ovalbumin concentration.....	78
28.	Solution density plotted as a function of RNase A concentration	79
29.	Solution viscosity plotted as a function of HEL concentration.....	82
30.	Solution viscosity plotted as function of STI concentration	82
31.	Solution viscosity plotted as a function of Dextran concentration	83
32.	Solution viscosity plotted as a function of Ovalbumin concentration.....	83
33.	Solution viscosity plotted as a function of RNase A concentration.....	84
34.	Sedimentation of Alexa488-BSA in buffer, Dextran, Ovalbumin and HEL ..	86

ABSTRACT

APPLICATIONS OF FLUORESCENCE DETECTED SEDIMENTATION

- I. STUDYING THE THERMODYNAMIC IMPACT OF VALENCE IN NON-IDEAL SOLUTIONS
- II. HIGH AFFINITY INTERACTIONS AND BIOLOGICAL MEDIA

By

Rachel R. Kroe

University of New Hampshire, December, 2005

The recent addition of the fluorescence detection optical system (FDS) to the currently available absorbance and interference optical systems on the analytical ultracentrifuge has greatly expanded the wide application of this technique. The new FDS is able to detect very low concentrations of fluorophore allowing the study of high affinity interactions ($K_d \sim \mu\text{M}$) not previously accessible with the absorbance optics. The types of high affinity interactions that can be explored include drug-protein interactions, lipid-receptor interactions, DNA-protein interactions and protein-protein interactions. Selective labeling of one or both of the macromolecules can allow elegant dissection of complex assemblies. The only limiting factor is the researcher's ability to label the macromolecule of interest. In addition to high affinity interactions, selective labeling of the macromolecule of interest with either a synthetic fluorophore or GFP allows study of sedimentation, diffusion and association in complex mixtures such as lysates, serum and other biological milieu. The use of FDS to study of complex mixtures has application in both the pharmaceutical and food

science industries. Finally, the ability to study macromolecules under non-ideal solution conditions will bridge what we know about macromolecular diffusion and assembly under ideal conditions and what has been learned about diffusion and assembly in the context of intact cells. New findings in this area will help to build upon what is already known about macromolecular crowding and aid in the refinement of current crowding theory. Examples of the applications listed above will be presented highlighting a diversity of systems and the power of this exciting new advancement in analytical ultracentrifugation.

CHAPTER I

INTRODUCTION

Most of our current understanding of biochemical equilibria, kinetics and thermodynamics is based on measurements that have been made in idealized solutions. Biochemists are trained to design experiments where the solution is dilute, homogenous and well defined. While most biochemists will concede that these conditions do not adequately describe the reality of biological media, technological and theoretical limitations require these assumptions. There is a growing interest in the scientific community to better understand the complexity of biological media and its impact on biochemical equilibria and reaction rates (Special Issue Jour. Mol. Rec). New technological advances currently emerging in the field of biochemistry will play an important role in expanding our understanding of this subject.

The cytoplasm of the cell and other biological media such as human plasma differ greatly from the idealized solutions constructed by scientists *in vitro*. Rather than being infinitely dilute, biological media contains a variety of macromolecular species such as membranes, proteins, ribosomes, DNA and RNA. While none of these macromolecules are individually present at high concentrations, taken together they occupy approximately 20-30% of the

volume of the cell (Hall, 2003; Minton, 1992). Due to this high macromolecular content the inside of cells are often referred to as being 'crowded' or 'volume occupied'.

The crowded environment of biological media has affects on both the kinetics and thermodynamics of the reactions occurring within the cell (Zimmerman, 1993; Hall, 2003). One effect of crowding is a reduction in the volume available for diffusion. The volume available for each macromolecule to diffuse in will depend on the size, number and shape of all the other molecules in the solution. Diffusion rates in crowded solutions are also affected by non-specific interactions that occur between various macromolecules along the diffusion path. Types of interactions that can slow or speed diffusion include steric-repulsive, hydrophobic, van der Waals and electrostatic. These types of non-specific interactions depend primarily on the global properties of the macromolecules such as net charge, dipole moments, polarity of the surface residues and macromolecular shape (Minton, 2001).

Current theories aimed towards describing the thermodynamics and kinetics of molecules in crowded solutions have focused primarily on the role of size, shape and steric-repulsive forces (Minton, 1998; Ellis, 2001). These theories define each macromolecule in terms of the hard spherical volume that it occupies in the cell. The volume available for each hard spherical macromolecule to occupy in a crowded solution is defined as the fraction of the

total volume that can be occupied by the center of that molecule. By this definition the volume that each macromolecule can occupy will be less than the total available volume in the solution. As a result the effective concentration of each macromolecule will be much higher than the actual concentration in the crowded medium. This increase in effective concentration will be greater for large macromolecules than it is for small macromolecules. The extent to which reaction rates and equilibria are altered by changes in effective concentration ultimately will be dictated by the size of the interacting molecules.

The above theory is often referred to as excluded volume theory. Excluded volume theory predicts that the crowded environment favors the formation of complexes. Favorability is predicted based on calculations of activity coefficients which can deviate from one by several orders of magnitude in solutions of physiological levels of volume occupancy. In practice, reaction rates have been experimentally measured to improve by up to 2 to 3 orders of magnitude in crowded solutions (Minton, 2001; Ellis, 2001). This enhancement in interaction affinity is not only a function of the high effective concentration of the macromolecules but also of the concomitant decrease in the total free energy of the solution. Other cellular processes predicted to be favored in a crowded environment include protein folding and the formation of inclusion bodies (Berg, 1999).

Experimentally the effects of excluded volume have been measured using methods such as tracer sedimentation equilibrium, fluorescence stopped-flow, fluorescence recovery after photo-bleaching, vapor pressure osmometry and freezing point depression. A tabulation of these studies can be found in reviews by Hall (2003) and Zimmerman (1998). The experimental results from most of these studies are consistent with predictions made by the excluded volume theory. However, in many of these studies the primary crowding agents are neutral inert macromolecules such as polyethylene glycol (PEG) or Dextran (Zimmerman 1998). Common proteins that are also used as crowding agents include Ovalbumin, Bovine Serum Albumin, Hemoglobin, Lysozyme and Ribonuclease. Interpretation of experimental results when proteins are used as crowding agents typically ignore the physical properties of these molecules such as net charge, dipole moments and surface polarity. The excluded volume theory assumes that all interaction enthalpies are equivalent. In practice it is commonly assumed that if working at physiological ionic strengths that the contribution of enthalpy to solution non-ideality will be small as compared to the entropy of the solution. It remains, however, that very little data exists on the role of charge in highly concentrated solutions.

The goal of this research is to examine the thermodynamic consequences of non-specific charge driven interactions on macromolecular mobility and reaction equilibria in high concentration solutions. Adding the second dimension of valence to current crowding theories will bring us one step closer to being able

to extrapolate the observations made in dilute solution to the context of a cell or complete organism.

Towards our research goal a series of tracer sedimentation velocity experiments has been designed in both high concentrations of a single background macromolecule and real biological media. In tracer sedimentation experiments a dilute macromolecular solute fluorescently or radioactively tagged is centrifuged in a high background of crowding agent or biological media (Rivas, 2003). The development of fluorescence detection (FDS) in the analytical ultracentrifuge has greatly expanded the utility of this method. In the experiments presented here green fluorescent protein (GFP), Alexa488 labeled bovine serum albumin (BSA) and Alexa488-IgG are used as tracer molecules. The fluorescence optics allow us to monitor the sedimentation of a tracer molecule independent of the complexity of the solution.

This research is divided into two parts. In the first part, experiments will be discussed where a tracer molecule is sedimented in high concentrations of background macromolecules of similar, opposite and neutral charge. The second part of this work will explore additional applications of FDS including sedimentation in biological media i.e. *E. coli* lysates and human serum.

CHAPTER II

MATERIALS AND METHODS

Materials

Chemicals

Tris hydrochloride, Potassium Chloride (KCl), Sodium Chloride (NaCl), and Ethylenediaminetetraacetic acid (EDTA) were purchased from Sigma.

Commercially Available Macromolecules

Hen egg white Lysozyme (L-6876, Lot 093K1455, $E_{280} = 37,470 \text{ cm M}^{-1}$, MW = $14,313 \text{ g mole}^{-1}$), Ovalbumin (A7641, Lot 071K7094, $E_{280} = 31,400 \text{ cm M}^{-1}$, MW = $42,750 \text{ g mole}^{-1}$), Dextran (D9260, Lot 093K0709, MW = $8,500 - 11,500 \text{ g mole}^{-1}$), and Soybean Trypsin Inhibitor Type 1-S (T-9003, Lot 074K7009, $E_{280} = 16,960 \text{ cm M}^{-1}$, MW = $20,095 \text{ g mole}^{-1}$) were purchased from Sigma. RNase A (78020Y, Lot 115588-017, $E_{280} = 8,940 \text{ cm M}^{-1}$, MW = $13,690 \text{ g mole}^{-1}$) was purchased from USB. Polyethylene Glycol 20,000 was purchased from Avocado Research Chemicals (25322-68-3). The concentrations of protein solutions were determined by measuring solution absorbance at 280 nm using the molar extinction coefficients listed above. The concentrations of the Dextran solutions were measured using a Reichert Abbe Mark II refractometer and $dn/dc = 0.15 \text{ ml/g}$.

Expression and Purification of Green Fluorescent Protein (GFP)

The GFP clone was a kind gift from Dr. Eric Schaller (Dartmouth). This clone of GFP contains multiple mutations (S65T, Q80R, F99S, M153T, V163A) and a hexa-histidine tag followed by a thrombin cleavage site for removal of the HIS-tag after purification. A T7 tag follows the thrombin cleavage site. The clone is inserted in a pET28a plasmid at the SacI and BamHI restriction sites. Plasmid DNA had been previously isolated by Jon Kingsbury in our laboratory and was used to transform BL21 DE3 bacteria selecting for Kanamycin resistance. A single colony was selected and used to inoculate a 25 ml culture of LB media containing 100 µg/ml of Kanamycin (Bristol Laboratories). This culture was grown at 37 °C overnight. A 2 liter flask containing 500 mls of LB media (3002-075, BIO101, Inc), with 100 µg/ml of Kanamycin was inoculated with 1 ml of the 25 ml culture and placed in a shaker at 37 °C. The OD of the culture was monitored and at 0.5 OD the culture was induced with 1 mM Isopropyl β-D-Thiogalacto Pyranoside (IPTG) (I-6758, Sigma). The bacteria were harvested 5 hours after induction and stored at -20 °C.

The GFP was purified in batch mode using Qiagen nickel resin by a standard method outlined in the Qiagen handbook. Briefly, the GFP pellet was thawed on ice and suspended in a pH 7.9 buffer containing 10 mM Tris, 250 mM NaCl, and 5 mM Imidazole (I-0125, Sigma). The solution was sonicated to lyse the cells and centrifuged at 11,000 RPM for 20 minutes. The supernatant was recovered after centrifugation and filtered through a 0.45 µm sterile filter. The

filtered supernatant was then added to the Qiagen nickel resin and mixed on an inversion mixer for 4 hours at 4 °C. The resin was then gently centrifuged and washed 3 times with a pH 7.9 buffer containing 20 mM Tris, 500 mM NaCl, and 10 mM Imidazole. GFP was eluted from the resin with a pH 7.9 buffer containing 20 mM Tris, 500 mM NaCl, and 1 M Imidazole. After elution the protein was dialyzed exhaustively into a pH 7.5 buffer containing 10 mM Tris, 100 mM KCl and 0.5 mM EDTA. The concentration of GFP solutions was determined using the molar extinction coefficient $E_{280} = 21,890 \text{ cm M}^{-1}$. The sequence molecular weight of GFP is $30,838 \text{ g mole}^{-1}$. The partial specific volume of GFP has been measured experimentally in our lab (Sarah Bean, Senior Thesis) and found to be 0.738 ml g^{-1} .

Expression and Purification of Barstar

The Barstar gene was cloned into a pET22b plasmid using the NdeI and HindIII restriction sites and transformed into BL21 DE3 (Gold) bacteria in the laboratory of Dr. Edward Eisenstein (CARB). This clone of Barstar contains two mutations (C40A and C82A) and a c-terminal hexa-histidine tag followed by a TEV protease cleavage site for removal of the HIS-tag after purification. The Barstar clone was given to our laboratory as a kind gift. Plasmid DNA was isolated from the BL21 DE3 (Gold) bacteria using a QIAprep Spin Miniprep kit and freshly transformed into BL21 DE3 bacteria selecting for Ampicillin resistance. A single colony was selected to inoculate 500 ml of Novagen Overnight Express Autoinduction media containing 100 µg/ml of Ampicillin and placed on a shaker

at 37 °C. After 17 hours the bacteria were harvested and the pellet was stored at -20 °C. A total of 5 Liters of culture was produced. Each Barstar pellet was purified in batch mode using the same method as listed above for GFP. The concentration of Barstar solutions was determined using the molar extinction coefficient $E_{280} = 22,460 \text{ cm M}^{-1}$. The sequence molecular weight of Barstar is $12,180 \text{ g mole}^{-1}$.

Recombinant soluble endothelial Protein C receptor (rsEPCR)

rsEPCR was a kind gift from Eli Lilly. The molar extinction coefficient of rsEPCR is $E_{280} = 29,910 \text{ cm M}^{-1}$. The molecular weight of rsEPCR is $32,490 \text{ g mole}^{-1}$.

Antibodies

Anti-GFP(FL) rabbit polyclonal IgG (Santa Cruz, sc-8334), anti-GFP mouse monoclonal IgG (Molecular Probes, A-11121), anti-GFP mouse monoclonal IgG (Zymed, 33-2600), anti-GFP mouse monoclonal IgG (BD Biosciences, 8362-1) and anti-GFP rat monoclonal IgG (MBL, D153-3) were purchased from vendors as indicated.

Fluorescently labeled Lipids and Proteins

1-Palmitoyl-2-{12-[(7-nitro-2-1,3-benzoxadiazol-4-yl) amino] dodecanoyl}-sn-Glycero-3-phosphocholine (DPPC-NBD) catalog number 810131 and 1,2-Dioleoyl-sn-Glycero-3-Phosphoethanolamine-N-(Carboxyfluorescein) (DPPE-

Fluorescein) catalog number 810332 were purchased from Avanti-polar lipids. Alexa-488 BSA (A13100) and Alexa488-IgG (A11034) were purchased from Molecular Probes.

Isolation of Human Serum and Plasma

Human blood (5 x 8mls) was collected into clot-activator tubes. The tubes were centrifuged in a clinical centrifuge to pellet the red blood cells and approximately 20 mls of serum was collected. Human blood (4 x10mls) was also collected in tubes containing heparin. The tubes containing heparin were centrifuged in a clinical centrifuge and approximately 30 mls of plasma was collected.

Methods

Sedimentation Velocity (absorbance optics)

rsEPCR: Sedimentation velocity data was collected for 14 uM rsEPCR at 20°C in a pH 7.5 buffer containing 20 mM Tris, 100 mM NaCl and 3 mM CaCl₂. Data was collected at 60,000 rpm using an 4-hole An60 Ti rotor. The sample was loaded into a SEDVEL60K centerpiece with quartz windows. Data was collected at 280nm.

Fluorescence Detection System (FDS) Instrumentation

Lasers: Experiments conducted prior to November 11, 2004 (See Appendix IX for dates of experiments) were performed using a Novalux Proterra

laser. The Novalux laser has a peak wavelength in the range of 486-490 nm with an output power of 15 mW. The protective coating on the base infrared Novalux laser was found to be highly sensitive to IR degradation under vacuum. As a result the majority of data collected with these lasers were collected at an output of 10 mW or less. When necessary, the power output was adjusted by a manual reconfiguration. Use of the Novalux laser was abandoned in November of 2004 and the switch was made to the Picarro Cyan laser. The Picarro laser has a wavelength of 488 nm +/- 0.5nm and varying output powers. Most units have an output power of approximately 10 mW.

Filters: The FDS optics prior to April 21, 2005 was configured such that the excitation light would pass through an assembly of lenses and then through a 100 μm spatial filter. Emitted light was detected by a PMT after passing through 490 nm high pass cut-off filter and a 600 μm spatial filter. After April 21, 2005 the spatial filter on the PMT side was reduced to 100 μm and the 490 nm filter was replaced with a 500 nm cut off filter. Reducing the size of the pinhole in the spatial filter and changing the cut off filter reduced the detected background signal and greatly improved the quality of data collected.

Photomultiplier Tube (PMT): The PMT used to detect the fluorescence emission signal is a Hamamatsu H6779-04. The sensitivity of each PMT varies from unit to unit. Unfortunately, the specific PMT installed in the FDS optics was not tracked over the course of these experiments. Therefore the values

below represent the best and worst case scenarios. The sensitivity of a PMT is determined by three parameters; cathode luminous sensitivity, anode luminous sensitivity and anode dark current. The cathode luminous sensitivity is a measure of the efficiency of the PMT to convert photons into electrons. The cathode luminous sensitivity range for the PMTs used in the various development optics ranges from 99 – 196 A/lm. The anode luminous sensitivity is a measure of the output current of the PMT after the secondary electron emission, also referred to as the gain. The gain on the various PMTs used in the development optics ranges from 54.7 -113 μ A/lm. The anode dark current is a measure of the current from the PMT when there are no incident photons. This is referred to as the 'noise' on the PMT. The background noise of the various PMTs ranged from 0.31 – 1.4 nA.

Software: Data collected prior to 2005 was collected using the beta version of the FDS software. Data collected after 2004 was collected with versions 1 through 1.932. The specific version used for each experiment was not tracked.

FDS Sedimentation Velocity

FDS of GFP in the presence of varying concentrations of background molecules (Dextran, Soybean trypsin inhibitor and hen egg white Lysozyme): Fluorescence detected sedimentation velocity studies were carried out at 20°C in a pH 7.5 buffer containing 10 mM Tris, 100 mM KCl and 0.5 mM EDTA. Data

was collected at 50,000 rpm using an 8-hole An50 Ti rotor. Samples were loaded into both the sample and reference sides of double sector SEDVEL60K or Beckman charcoal-filled epon centerpieces. For experiments where HEL and STI served as background material, data was collected for 40 nM GFP in background concentrations ranging from 0.75 to 50 mg ml⁻¹. For the Dextran experiments data was collected for 40 nM GFP in background concentrations ranging from 0.07 to 35.3 mg ml⁻¹. All background molecules were dialyzed exhaustively against buffer prior to the addition of GFP. Both quartz and sapphire windows were used.

Data was analyzed using SEDFIT version 8.9 (available online at www.analyticalultracentrifugation.com, Schuck, 2000). The data were fit with multiple models including the non-interacting discrete species model, continuous c(M) model and the continuous c(s) model. The details of how each of these fits was performed are indicated below. Data fits for GFP sedimenting in dextran, STI and HEL were first performed using the non-interacting discrete species model fitting for S_{app} , D_{app} , C_{app} , time-independent (TI) and radially invariant (RI) noise. For each fit 68.3% confidence intervals were calculated, using the sedfit software, for both S_{app} and D_{app} fit values. Apparent S and D values were corrected to $S_{20,W}$ and $D_{20,W}$ values using measured density and viscosity values as reported in appendices III and IV. A second fit to the data was performed using the continuous molar mass distribution model. For these fits the density of the solution, the viscosity of the solution and the partial

specific volume of GFP were specified. The experimental data was fit with a resolution of 100 over a range of 10,000 to 100,000 g mol⁻¹ fitting for TI and RI noise allowing the f/f_0 ratio to float. Monte Carlo analysis using 100 simulations over an integrated weight average range of molecular weight values was performed to estimate the error on the fit molecular weights from these analyses. The ratio of apparent concentration to the true concentration, the activity of the solution, was calculated and the ratio of the sequence molecular weight of GFP divided by the fit molecular weight.

Data fits were also performed using the continuous $c(s)$ model. The experimental data were fit with a resolution of 100 over a range of 0.5 to 6 S fitting for TI and RI noise. Monte Carlo analysis using 100 simulations over an integrated weight average range of S values was performed to estimate the error on the fit sedimentation coefficients from these analyses.

FDS of DPPC-NBD in the presence and absence of rsEPCR:

Fluorescence detected sedimentation velocity studies were carried out at 20°C in a pH 7.5 buffer containing 20 mM Tris, 100 mM NaCl and 3 mM CaCl₂. Data was collected for 400 nM NBD-DPPC in 10, 5, 2.5 and 1.25 μM rsEPCR at 60,000 rpm using an 4-hole An50 Ti rotor. Samples were loaded into both the sample and reference sides of double sector SEDVEL60K centerpieces with sapphire windows. The data were fit using Sedfit version 8.9 using both the continuous $c(s)$ distribution and non-interacting discrete species models fitting

for TI and RI noise. Error analysis was performed on the discrete species fits calculating the 68.3% confidence intervals for the S_{app} fit value.

FDS of GFP and Anti-GFP: Anti-GFP (MBL) was dialyzed against a pH 7.5 buffer containing 10 mM Tris, 100 mM KCl and 0.5 mM EDTA at 4 °C to remove the 50% glycerol from the antibody solution. After dialysis the antibody was serially diluted 1:3 into buffer covering an antibody concentration range of 540 to 0.003 nM. A concentration of 40 nM GFP was added to each of the antibody dilutions. Cells were assembled with double sector charcoal-epon and SEDVEL60K centerpieces with either quartz or sapphire windows. Data were collected at 20 °C and 50,000 rpm in an 8-hole An50 TI rotor. The data were fit using SEDFIT version 8.9 using the continuous $c(s)$ distribution fitting for TI and RI noise. Monte Carlo analysis using 100 simulations over an integrated weight average range of S_{app} values was performed to estimate the error on the fit sedimentation coefficients from these fits.

FDS of Alexa488-BSA and Alexa488-IgG: Alexa488-BSA was re-suspended into a pH 7.5 buffer containing 10 mM Tris, 100 mM KCl and 0.5 mM EDTA. Data was collected at 20 °C and 50,000 rpm in a 8-hole An50 Ti rotor for 500 nM Alexa488-BSA in buffer, 1.4 nM Alexa488-IgG in buffer, 100 nM Alexa488-BSA in human serum and plasma and 100 nM Alexa488-IgG in human serum and plasma. Cells were assembled with quartz windows and either double sector charcoal-epon or SEDVEL60 centerpieces. The data were

fit using SEDFIT version 8.9 using the continuous $c(s)$ distribution fitting for TI and RI noise. Monte Carlo analysis using 100 simulations over an integrated weight average range of S_{app} values was performed to estimate the error on the fit sedimentation coefficients from these fits.

FDS of GFP in serum: GFP was spiked into human serum at GFP concentrations ranging from 540 to 4 nM. In a second set of experiments, human serum was serially diluted 1:2 in buffer from 100% to 0.05% at a constant concentration of 40 nM GFP (data not discussed). Data was collected at 20 °C and 50,000 rpm in a 8-hole An50 Ti rotor. The cells were assembled with double sector charcoal-epon centerpieces and quartz windows. The low concentration GFP data were fit using SEDFIT version 8.9 using both the continuous $c(s)$ distribution fitting for TI and RI noise.

FDS of GFP and anti-GFP in serum: Equal concentrations (100 nM) of GFP and anti-GFP (MBL) were spiked into human serum. Data was collected at 20 °C and 50,000 rpm in a 8-hole An50 Ti rotor. The cells were assembled with double sector charcoal-epon centerpieces and quartz windows. The low concentration GFP data were fit using SEDFIT version 8.9 using both the continuous $c(s)$ distribution fitting for TI and RI noise. Monte Carlo analysis over an integrated weight average range of S_{app} values was performed using 100 simulations to estimate the error on the fit sedimentation coefficients.

FDS of fluorescein-DPPE in serum: Human serum was spiked with either 4 μM or 2 μM fluorescein-DPPE. Data was collected at 20 °C and 50,000 rpm in a 8-hole An50 Ti rotor. The cells were assembled with double sector charcoal-epon centerpieces and quartz windows. The data shown in chapter 4 is at the 4 μM concentration.

FDS of GFP in E.Coli Lysates: The E. Coli lysates used in these experiments were obtained during the purification of Barstar (see above). For these experiments the bacteria were lysed in a pH 7.9 buffer containing 20 mM Tris, 500 mM NaCl, and 10 mM Imidazole. After sonication the lysate was dialyzed overnight at 4 °C into a pH 7.5 buffer containing 10 mM Tris, 100 mM KCl and 0.5 mM EDTA. After dialysis, the total protein concentration of the lysate was measured using a Biorad protein assay (catalog # 500-0002) and found to be 6.8 mg/ml. A concentration of 20 nM GFP was spiked into various dilutions of the E. Coli lysate ranging from 6.8 to 0.1 mg/ml total protein concentration. Data was collected at 20 °C and 50,000 rpm in a 8-hole An50 Ti rotor. The cells were assembled with double sector charcoal-epon centerpieces and quartz windows. The data were fit using Sedfit version 8.9 using the continuous c(s) distribution fitting for TI and RI noise.

Fluorescence Polarization: For the polarization experiment the concentration of the anti-GFP (MBL, D153-3) was determined using a Biorad protein assay (catalog # 500-0002). The experiment was set up in the 96-well

Dynex (#7005) round bottom low-binding black polystyrene plate. Anti-GFP was added to the first two wells of rows 1-2 at a concentration of 2 μ M and serially diluted across the plate 1:2 in 100 μ l of a pH 7.5 buffer containing 10 mM Tris, 100 mM KCl and 0.5 mM EDTA. Next, 100 μ l of a 2 nM GFP stock solution in the same buffer was added to all of the wells such that the final concentration of GFP in all the wells was 1 nM. The concentration of the antibody ranged from 1 μ M to 200 pM. Fluorescence polarization was measured using an LJL platereader (Ex 485 nm, Em, 530 nm) with a 561 nm dichroic mirror installed. The data were fit using a program written in SAS for fitting direct one site binding fluorescence polarization data.

CHAPTER III

GFP AS A PROBE OF NON-IDEALITY IN HIGH CONCENTRATION BACKGROUNDS

Introduction and Theory

The colligative properties of a solution provide a measure of the chemical potential of the solvent in the solution relative to that of pure solvent (Tanford, 1961). Osmotic pressure, vapor pressure, freezing point depression and boiling point elevation are all colligative properties. Experimentally these properties can be used to determine the molecular weight of the solute. In particular, osmotic pressure (Π) can be used for determining the mass of solute molecules such as proteins. Typically this is done by measuring osmotic pressure at several concentrations (C_B) of the macromolecule and constructing a plot of Π/C_B versus C_B . In this type of plot, the reciprocal intercept on the y-axis yields a value for the apparent molecular weight of the macromolecule. Measurement of the colligative properties of a solution, such as osmotic pressure, captures the sum effect of all the forces present in a solution (Tanford, 1961). As solutions become more concentrated, effects such as excluded volume, charge-charge interactions, dipole interactions, and surface polarity will alter solution properties causing them to behave non-ideally. For this reason, extrapolation to an infinitely dilute solution is required to acquire a precise value for the macromolecule's molecular weight.

Mathematically, deviations from ideality are taken into account by writing a virial expansion of the van't Hoff equation:

$$\frac{\Pi}{C_B} = RT\left(\frac{1}{M_B} + Bc.....\right) \quad (1)$$

where Π is the osmotic pressure, C_B is the molar concentration, R is the gas constant, T is the temperature, M_B is the molecular weight and B is the second virial coefficient. The second virial coefficient describes the non-ideality of the solution. Experimentally, the second virial coefficient is measured as the slope of a Π/C_B versus C_B plot, which for an ideal solution would be zero. Deviations from zero slope can be either positive or negative depending on the nature of the forces present in the solution. If the interactions between the solution components are primarily repulsive, the value of B will be positive. If the components in the solution are associating and/or other weak favorable interactions are occurring in the solution, the value of B will be negative.

While measuring the osmotic pressure of a solution directly provides the sum value of B , the contributions of factors influencing deviations from ideality can be estimated mathematically. The contribution of excluded volume can be estimated using equation 2:

$$B = \frac{16\pi N r^3}{3M_B^2} \quad (2)$$

where N is Avogadro's number, r is the radius of the macromolecule and M_B is the molecular weight of the molecule (Tanford, 1961). The contribution of charge-charge interactions can be estimated using equation 3:

$$B = \frac{z^2}{4M_B^2c} \quad (3)$$

where z is valence, M_B is molecular weight and c is concentration (Tanford, 1961). This value is also referred to as the Donnan term.

The predicted osmotic pressure of concentrated macromolecule solutions can be calculated using equation 1 taking into account the contributions of excluded volume and charge to the second virial coefficient. The impact of these two forces on the solution properties can be visualized by constructing a graph of C_{app}/C versus concentration; where C_{app} is the concentration calculated from the predicted osmotic pressure and C is the true concentration of the macromolecule solution. The ratio of C_{app}/C is often referred to as the 'activity' of a solution. The squares in Figure 1 show the expected ratio of C_{app}/C for an ideal solution. In an ideal solution the measured concentration will always reflect the absolute concentration of the solution. The diamonds in Figure 1 show the calculated effect of both excluded volume (Equation 2) and charge-charge interactions (Equation 3) on the activity of hen egg white Lysozyme (HEL) in a buffer at physiologically relevant ionic strength (0.11 M) and pH (7.5).

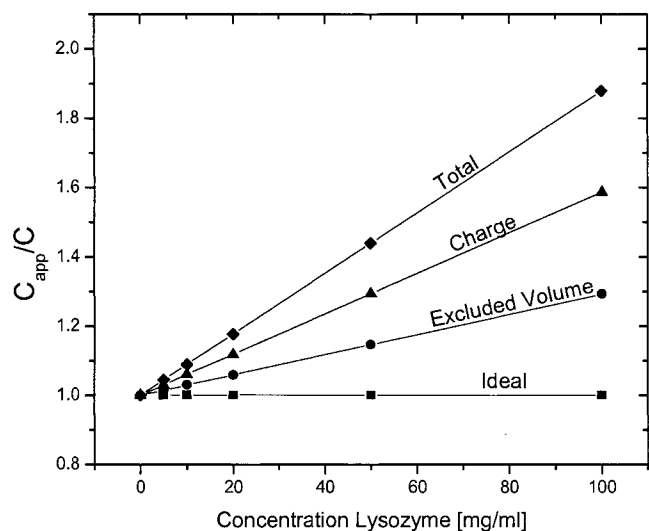


Figure 1: Predicted effect of excluded volume (circles) and charge (triangles) on the total (diamonds) activity of HEL in high concentrations of HEL.

As a result of excluded volume and charge-charge interactions the activity of the HEL solution is predicted to increase as the concentration of HEL increases. The extent to which this increase is influenced by excluded volume and charge are shown by the circles and triangles respectively. It can be seen that the contribution of charge-charge repulsion to solution non-ideality is greater than the contribution of excluded volume. This graph shows that charge-charge repulsion is a significant force contributing to the non-ideality of high concentration solutions at physiologically relevant salt concentrations.

The goal of this research is to experimentally characterize the impact of non-specific charge-charge interactions that occur in concentrated solutions. To

address this goal a series of tracer sedimentation velocity experiments were constructed using the fluorescence detection system in the analytical ultracentrifuge. In these experiments GFP is sedimented in concentrated solutions of anionic, cationic and neutral macromolecules. Tracer sedimentation provides a means of measuring changes in the apparent molecular weight of the GFP and thus the activity of the solution that occurs as a result of the non-ideality of high concentrations of macromolecules of varying charge.

The sedimentation velocity data discussed in this research has been fit using several different models. At this time it is not clear how to best fit tracer sedimentation velocity data in concentrated solutions. Future analysis of this data with more appropriate fitting models will likely provide clearer insight into both the hydrodynamic and thermodynamic phenomena occurring in these solutions.

Results

The choice of biological standards to be used as background macromolecules was based on several criteria. First, the background macromolecules must have a mass less than that of the tracer molecule in order to avoid the manifestation of Johnston-Ogston effects in the sedimentation velocity data (Johnston, 1946; Correia, 1976). The choice of similar molecular weight background macromolecules also allows the phenomena observed in the

sedimentation velocity data to be explained primarily in terms of valence. Second, the background macromolecules should be well characterized and soluble enough to work with at high concentrations. Finally, it is important that the background macromolecules are not prohibitively expensive to work with in hundred's of milligram quantities.

Based on the above considerations, HEL, Soybean Trypsin Inhibitor (STI) and Dextran were selected to be used as background macromolecules. The valence of HEL, STI and GFP at pH 7.5 have been measured in our laboratory and found to be $z = +6.1 \pm 0.1$, $z = -8.6 \pm 0.3$ and $z = -6.4 \pm 0.3$ respectively (Sue Chase unpublished). Details of the measurement of the Stoke's radius for two of these macromolecules, used for the calculation of valence, can be found in Appendix I. Dextran is a neutral ($z = 0$) macromolecule.

Prior to conducting experiments in concentrated solutions the sedimentation of GFP was characterized in dilute solution. The $c(s)$ distribution for GFP at low concentration (40 nM) in buffer is shown as the green line in Figure 2. These data were collected using the FDS optics and fit to a $S_{20,w}$ of 2.87 (2.85, 2.89) and a molecular weight of 31,107 (31,072 – 31,113) g mole⁻¹. These results are consistent with GFP being a monomeric protein. GFP was also sedimented at higher concentrations (μ M) using the absorbance optics. The absorbance data fit to a $S_{20,w}$ of 2.90 (2.89, 2.91) and a molecular weight of 31,050 (30,842 – 31,219).

To explore the role of valence in concentrated solutions anionic GFP was first sedimented in solutions containing various concentrations of the neutral macromolecule Dextran. Collecting data using a neutral macromolecule provides a baseline for the contribution of excluded volume to the non-ideality of these solutions. The grey line in Figure 2 shows the $c(s)$ distribution for GFP sedimenting in a background of 35 mg ml^{-1} Dextran. The cartoon in the upper left hand side corner of Figure 2 illustrates the solution conditions. The molar concentration of Dextran ranges from 150 to 88,250 fold greater than GFP. The data show that the apparent sedimentation of GFP is slowed in the presence of Dextran.

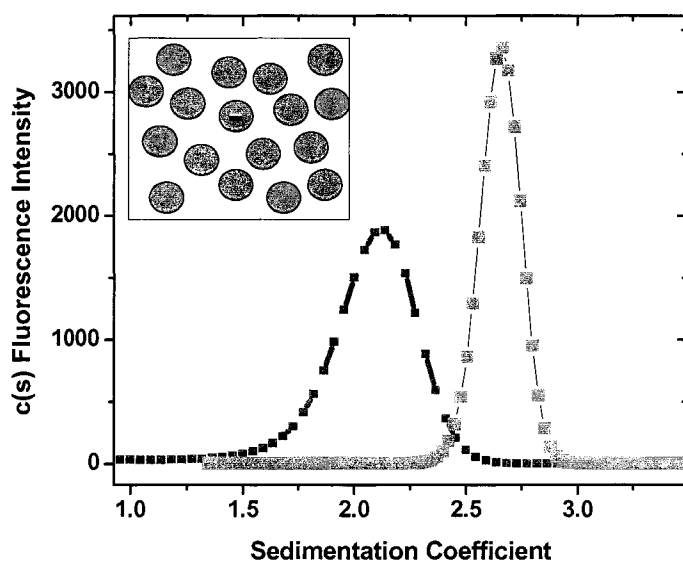


Figure 2: The apparent sedimentation of GFP in dilute solution (green) and in a background of 35 mg ml^{-1} Dextran (grey) in 10 mM Tris pH 7.5, 100 mM KCl, and 0.5 mM EDTA at 50,000 rpm and 20 °C.

The decrease in the apparent sedimentation of GFP is concentration dependent as shown in Figure 3. Correcting the apparent sedimentation coefficients using measured density and viscosity values (Appendix III and IV) reveals similar $S_{20,W}$ values at each concentration of Dextran (Figure 4). This would suggest that the shift in sedimentation coefficient is primarily a hydrodynamic effect resulting from the increased viscosity and density of the 35 mg ml⁻¹ Dextran solution. A similar phenomenon is observed when GFP is sedimented in a 50 mg ml⁻¹ solution of PEG 20K and is discussed in Appendix II.

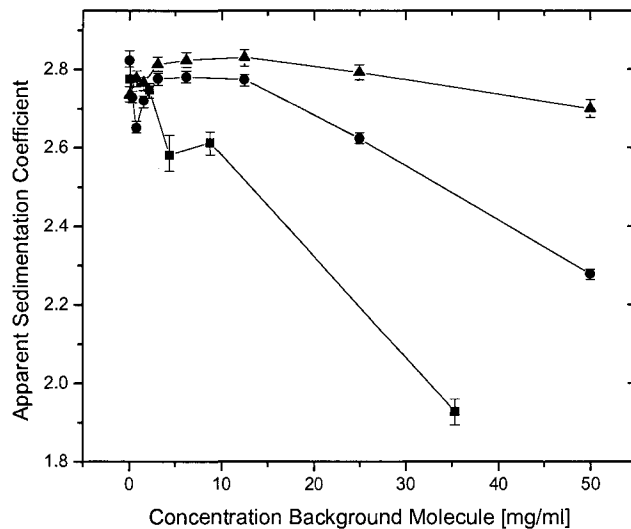


Figure 3: The apparent sedimentation coefficient of GFP in Dextran (squares), STI (circles) and HEL (triangles) as function of background molecule concentration in 10 mM Tris pH 7.5, 100 mM KCl, and 0.5 mM EDTA at 50,000 rpm and 20 °C. Data has not been corrected for solution density or viscosity.

Diffusion coefficients (D) also were fit and are shown as $D_{20,W}$ values in Figure 4. The error on the diffusion coefficient is significantly greater than the error on S . This is expected as it is more difficult to precisely fit for boundary spreading as compared to the midpoint of the boundary; however, some of the error in D is contributed in part by sub-optimal laser focus. The ratio of $S_{20,W}/D_{20,W}$, also plotted in Figure 4, is an indication of the trend in the apparent molecular weight of GFP as a function of Dextran concentration. The apparent molecular weight appears to remain constant throughout the concentrations of Dextran tested.

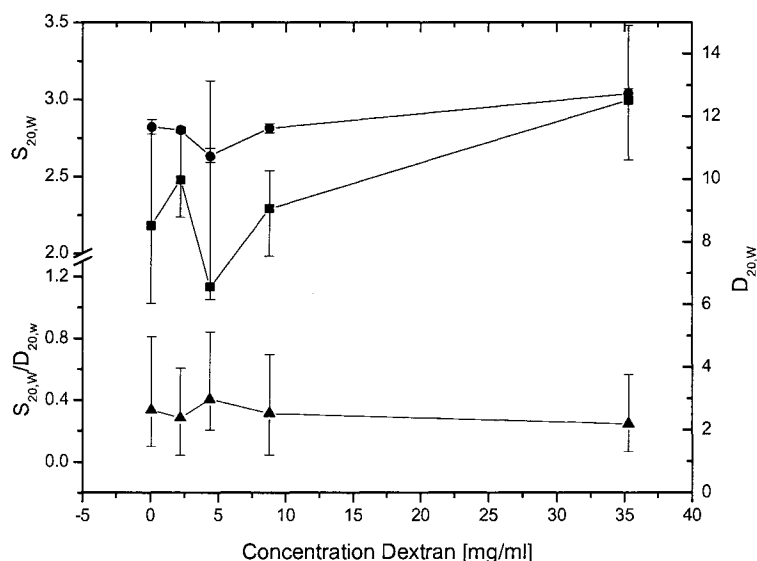


Figure 4: Calculated $S_{20,W}$ (black circles), $D_{20,W}$ (blue squares) and ratio $S_{20,W}/D_{20,W}$ (red triangles) of GFP as a function of Dextran concentration.

In the next set of experiments, data was collected to explore the effect of high concentrations of a background macromolecule of similar charge to GFP. In these experiments STI was used in place of Dextran. These experiments were

designed such that GFP would sediment in a nearly constant enthalpic bath. Figure 5 shows the $c(s)$ distribution of GFP in 50 mg ml^{-1} of STI. As seen in the Dextran solution, the sedimentation of GFP is slowed in high concentrations of STI (Figure 3). The sedimentation of GFP was measured in STI solutions covering molar concentrations ranges from 435 to 62,200 fold in excess of the concentration of GFP. The reduction in apparent sedimentation coefficient was shown to be concentration dependent (Figure 3). Similar phenomena of GFP sedimentation has also been observed using Ovalbumin as the anionic background molecule and is discussed in Appendix II.

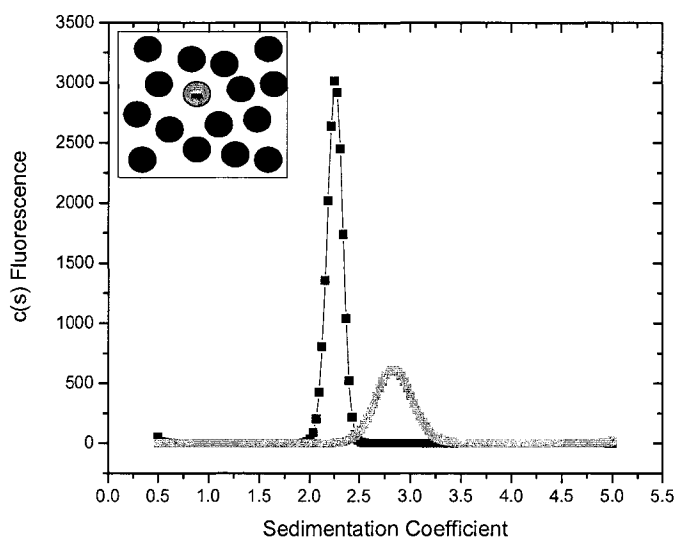


Figure 5: The apparent sedimentation of GFP in dilute solution (green) and in 50 mg ml^{-1} STI (red) in 10 mM Tris pH 7.5, 100 mM KCl, and 0.5 mM EDTA at 50,000 rpm and 20 °C.

Correction to $S_{20,W}$ values reveal a fairly constant value (Figure 6) suggesting that the shift in sedimentation coefficient is primarily a hydrodynamic effect. In contrast to the Dextran results, the $D_{20,W}$ value decreases as the concentration of STI increases. This decrease in D results in a small increase in the ratio of $S_{20,W}/D_{20,W}$ and thus a proportional increase in the apparent molecular weight of GFP at high STI concentrations.

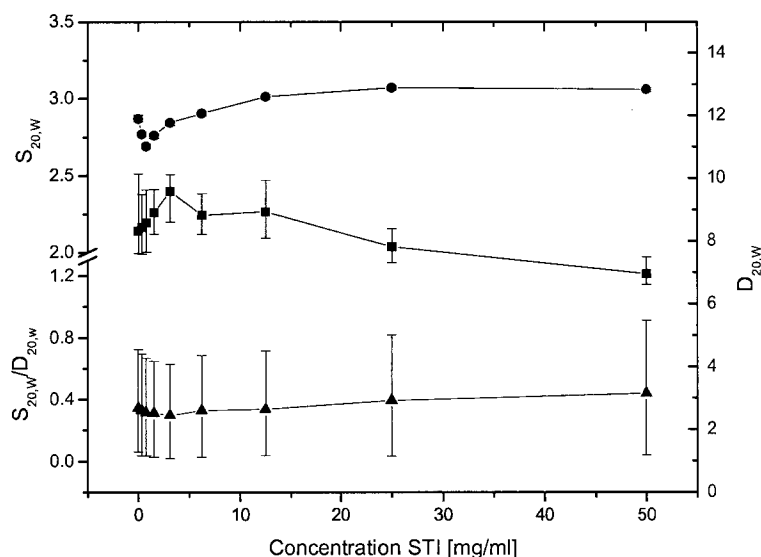


Figure 6: Calculated $S_{20,W}$ (black circles), $D_{20,W}$ (blue squares) and ratio $S_{20,W}/D_{20,W}$ (red triangles) of GFP as a function of STI concentration.

The third set of experiments examines how high a background concentration of a macromolecule of opposite charge affects GFP sedimentation. In these experiments HEL was used as the background macromolecule. Figure 7 shows the $c(s)$ distribution for GFP in 50 mg ml^{-1} HEL. Contrary to what is seen in the

neutral or same charge solutions the sedimentation of GFP is unchanged in the HEL backgrounds (Figure 3). Conversion to $S_{20,W}$ values shows that the sedimentation coefficient is increasing in the HEL solutions (Figure 8). Since similar phenomena was not observed in the Dextran and STI solutions it is unlikely that the increase in sedimentation coefficient is arising from simple hydrodynamic non-ideality or excluded volume. Instead, these data suggest that GFP may be co-sedimenting with the HEL as depicted in the cartoon in the upper left hand side of Figure 7. Similar to what was seen in the STI solutions the diffusion coefficient for GFP is shown to decrease as the concentration of HEL increases (Figure 8). The decrease in diffusion coefficient coupled with the increase in sedimentation coefficient results in a significant increase in apparent molecular weight of GFP in these solutions.

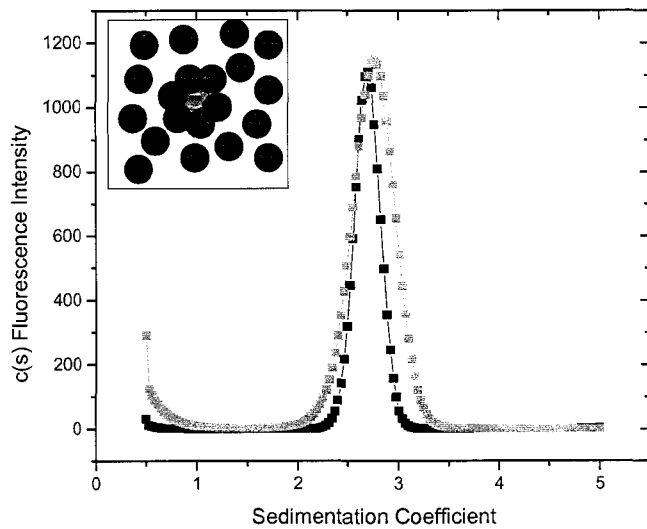


Figure 7: The apparent sedimentation of GFP in dilute solution (green) and in 50 mg ml⁻¹ HEL (blue) in 10 mM Tris pH 7.5, 100 mM KCl, and 0.5 mM EDTA at 50,000 rpm and 20 °C.

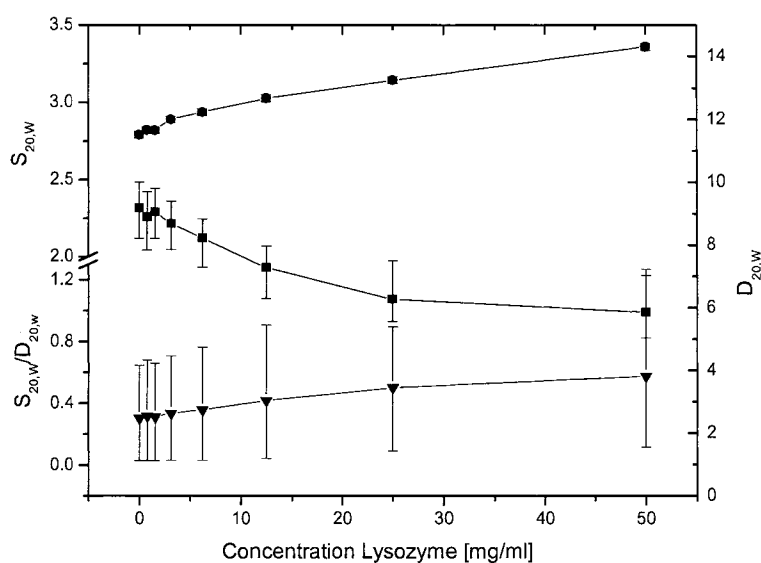


Figure 8: Calculated $S_{20,W}$ (black circles), $D_{20,W}$ (blue squares) and ratio $S_{20,W}/D_{20,W}$ (red triangles) of GFP as a function of HEL concentration.

This phenomenon has also been observed sedimenting Alexa488-BSA (anionic) in backgrounds of Ovalbumin (anionic), HEL (cationic) and Dextran (neutral) as discussed in Appendix V. The fact that similar observations have been made with both GFP and Alexa488-BSA suggest that the observed effects of valence may be generally applied and may not be unique properties of our choice of tracer or background molecules.

In order to better quantify the changes in the apparent molecular weight of GFP in the various solutions, the data were fit to a continuous $c(M)$ distribution model taking both viscosity and density of the solutions into account. The apparent molecular weights obtained as the peak in the $c(M)$ distributions from these fits

were used to calculate the activity of each solution. In Figure 9, the activity of each of the solutions is plotted as a function of background macromolecule concentration. The activity of GFP in the Dextran solutions appears to be constant over the concentration range tested. Interestingly, the activity of GFP in both the 50 mg ml⁻¹ STI and HEL is shown to decrease. This suggests the presence of weak attractive forces in these solutions.

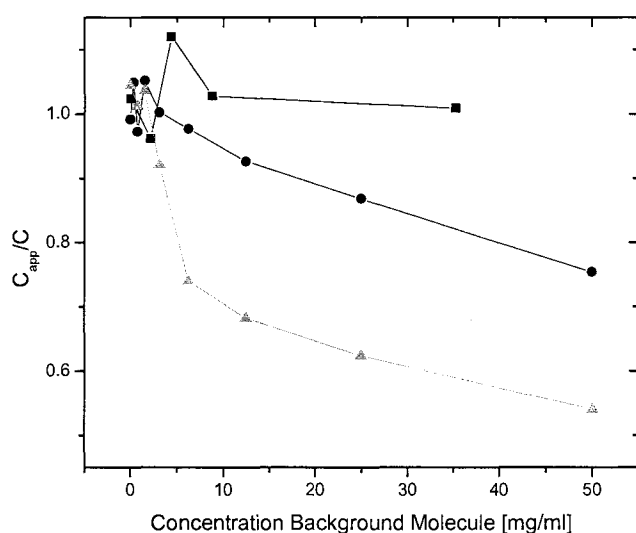


Figure 9: The activity of GFP as function of Dextran (Black squares), STI (red circles) and HEL (green triangles) concentration) in 10 mM Tris pH 7.5, 100 mM KCl, and 0.5 mM EDTA.

The Sedfit software allows the user to fit for the ratio of f/f_0 , where f is the frictional coefficient of the molecule being sedimented and f_0 is the frictional coefficient of a smooth compact sphere. The ratio of f/f_0 provides information about the shape of the GFP and the extent to which it is solvated. The ratio of

f/f_0 was allowed to float in the $c(M)$ fits. A graph of f/f_0 versus concentration of background molecules for GFP in each of the background solutions is plotted in figure 10. The ratio of f/f_0 is constant in the Dextran solutions. In the HEL solution the ratio of f/f_0 for GFP increases as function of HEL concentration. An increase is also observed in high concentrations of STI. One interpretation of these data is that the increase in f/f_0 is indicative an increase in the Stokes radius of the GFP. The increase in f/f_0 may also represent the extent to which the sedimentation of GFP is coupled to the sedimentation of the background molecule.

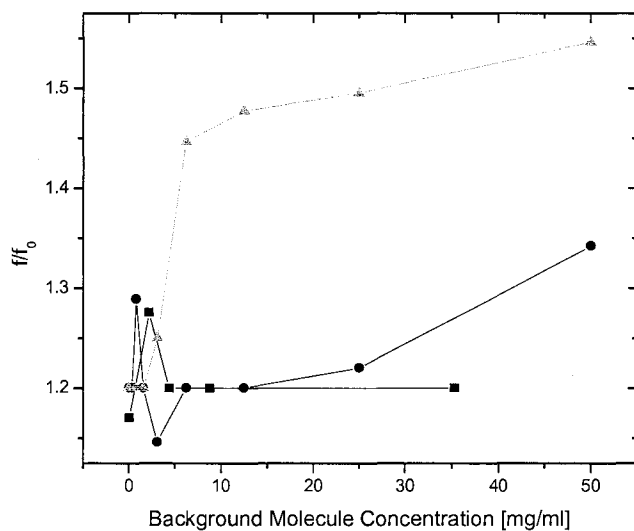


Figure 10: Ratio of f/f_0 for GFP in Dextran (black squares), STI (red circles) and HEL (green squares).

Discussion

As introduced earlier, predictions of the non-ideality of a solution can be calculated using the virial expansion of the van't Hoff equation. Similar calculations can be made to estimate the impact of excluded volume and charge-charge interactions occurring between the tracer molecule and the background molecules. Figure 11 shows the predicted impact of excluded volume and charge-charge non-ideality on the activity of GFP in each of the background solutions. Taking the solution non-ideality into account the van't Hoff equation predicts there to be little effect of high concentrations of Dextran on the activity of the GFP solutions. The experimental data confirm this prediction. Similar calculations made for the HEL solutions predict the decrease in activity measured for GFP in the HEL solutions. However, the predicted decrease in activity is not as great as what is measured experimentally. The shortcomings of these predictions become most obvious when a comparison is made between the predicted activity of GFP in the STI backgrounds and what is experimentally measured. The van't Hoff equation predicts that the activity of GFP to increase in the STI solutions, however a decrease is measured. Experimentally, the data for GFP in the HEL and STI solutions show that predictions made based on excluded volume and charge alone do not account for all of the phenomena occurring in these high concentration solutions.

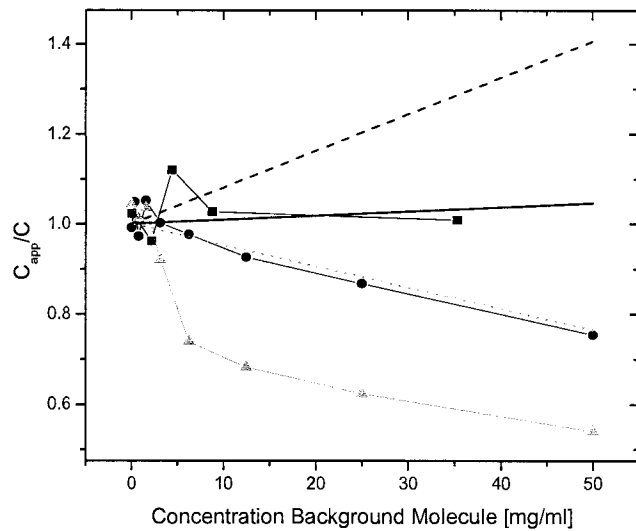


Figure 11: Calculated impact of solution non-ideality on the activity of GFP in Dextran (black line), STI (red dotted line) and HEL (green dotted line) as compared to experimentally measured values in Dextran (black squares), STI (red circles) and HEL (green triangles).



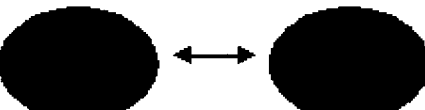
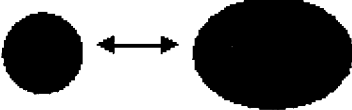
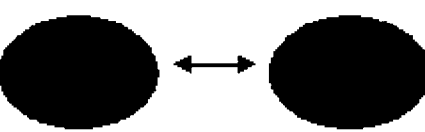
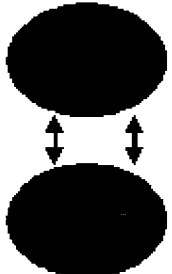
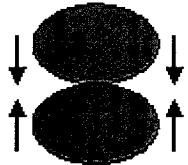
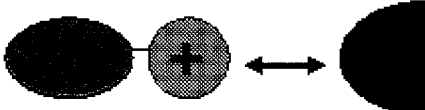
One possible explanation for the measured decrease in GFP activity could be that the GFP is forming a dimer. The model used for calculations made with the van't Hoff equation does not include the potential for dimer formation. However, GFP dimerization seems unlikely since there was no evidence of GFP dimerization in the sedimentation velocity experiments conducted at μM concentrations. In addition the data fit well to a single species model with no indication of an interaction boundary. Finally, if dimer formation were favored due to excluded volume effects, we would expect to see it in the Dextran solutions as well.

In our analysis we are considering the background molecules as having a single evenly distributed charge. In reality, these macromolecules have patches of charge that vary across the surface. It is possible that STI has a cationic patch that favorably interacts with the GFP at the higher concentrations. In fact, inspection of the electrostatic surface of the STI crystal structure shows a cluster of 3 cationic residues. The fact that GFP appears to co-sediment with STI at high concentrations may reflect the relative non-ideality of interactions between STI and itself as compared to interactions with GFP. Since STI is more highly charged than GFP, it will be more favorable for STI to co-sediment with GFP relative to another STI molecule. It is also possible that the effect seen in the STI solution is the result of another type of interaction driven by dipole moment or surface polarity. Additional favorable interactions such as these may also explain why the measured activity of GFP in the HEL solutions is greater than what is predicted.

Table 1 (reproduced from Matthews and van Holde) contains a list of all of the types of non-covalent interactions that can occur in solution. Charge-Charge interactions occur over the longest range distance and are the dominant forces at low to moderate concentrations. However, as solutions become more concentrated molecules will be more closely packed thus increasing the probability for other interactions such as charge-dipole, dipole-dipole and hydrogen bonding to occur. All of these interactions are favorable and would

result in a decrease in the activity of the solution. Our calculations using the van't Hoff equation do not take into account these additional favorable forces. The data suggest that these additional forces have a significant impact on the measured non-ideality of concentrated solutions.

Table 1: Non-covalent Interactions

Type of Interaction	Model	Dependence of Energy on Distance
Charge-Charge (Longest-range force, non-directional)		$1/r$
Charge-Dipole (Depends on orientation of the dipole)		$1/r^2$
Dipole-Dipole (Depends on mutual orientation of dipoles)		$1/r^3$
Charge-Induced Dipole (Depends on the polarizability of the molecule in which the dipole is induced)		$1/r^4$
Dipole-Induced Dipole (Depends on the polarizability of the molecule in which the dipole is induced)		$1/r^5$
Dispersion (Involves mutual synchronization of fluctuating charges)		$1/r^6$
Van der Waals Repulsion (occurs when outer electron orbitals overlap)		$1/r^{12}$
Hydrogen Bond (Charge attraction + partial covalent bond)		Length of bond fixed

The data generated thus far show that valence is a significant driving force for non-specific interactions in complex media. Experiments conducted where tracer molecules are dissolved in solutions containing high concentrations of macromolecules of defined charge show that the tracer molecule preferentially sediments with macromolecules of opposite charge. The data also show that as solutions become more concentrated the role of short-range non-covalent interactions becomes significant. More importantly these data highlight the need to consider not only the entropic but also the enthalpic forces present in high concentration solutions. An understanding of high concentration solutions is necessary to better understand the forces and organizing principles in complex media such as serum and cell lysates.

The addition of fluorescence optics to the analytical ultracentrifuge has expanded our ability to study the sedimentation in complex and concentration solutions. Future work will be aimed towards gaining a better understanding of the role of charge and weak attractive forces in concentrated solutions through use of the sedimentation equilibrium method. Sedimentation equilibrium data will allow us to dissect the features of the data that are the result of hydrodynamic non-ideality from thermodynamic non-ideality.

CHAPTER IV

APPLICATIONS OF FDS

One of the primary advantages to using fluorescence optics over either the absorbance or interference optics in the analytical ultracentrifuge is sensitivity. The fluorescence optics can detect fluorophores over a concentration range covering 6 to 8 logs. The lower limit of detection is dictated by multiple factors including the power of the lightsource (laser), the sensitivity of the photo multiplier tube (PMT) and the quantum yield of the fluorophore. If all of these factors are optimized, fluorophore concentrations in the pM to fM level can easily be detected (MacGregor, 2004; Laue, 2004). The ability to study the sedimentation behavior of macromolecules at such low concentrations enables experimenters to study high affinity interactions previously inaccessible with either the absorbance or interference optical systems. Examples of the application of FDS to study high affinity interactions will be discussed in this chapter (see examples 1-2).

The second major advantage to using fluorescence optics in the analytical ultracentrifuge is the ability to selectively monitor the sedimentation of a single component in a solution. Experiments of this type are often referred to as tracer sedimentation (Rivas, 2003). Tracer sedimentation can be applied to simple

two-component systems as discussed in example 1 as well as to highly complex systems such as the sedimentation of a macromolecule in serum or cell lysates. In this chapter several examples of the application of FDS to selectively monitor sedimentation in complex solutions will be discussed (examples 3-8).

When designing experiments to be conducted with the fluorescence optics the experimenter chooses to label the macromolecule of interest either chemically with a dye (Alexa488, fluorescein, Oregon green) or genetically by preparing a GFP fusion protein. In all cases control experiments should be done to confirm that the labeling procedure has not altered the physical properties of the macromolecule. This is most easily done by conducting competition experiments with an unlabeled version of the macromolecule of interest.

Another concern when working with fluorescence is photo-bleaching. The sensitivity of the labeled macromolecule to photo-bleaching over the time-course of the sedimentation experiment should be characterized and taken into account when analyzing data. Photobleaching of GFP and Alexa488, the two fluorophores discussed in this chapter, has not been exhaustively studied. However, it was generally not found to be a problem.

The experiments presented in this chapter were performed using FDS detectors and software in various states of development. There have been several designs of fluorescence detectors for the analytical ultracentrifuge over the years (MacGregor (2004) and therein). Brief details of the detectors used in

these studies are covered in chapter 2. A complete description of the latest detector will be covered elsewhere (Laue, Austin, Rau in press and in preparation).

As a final note, all of the work covered in this chapter is still in progress. The goal of this chapter is to highlight the use of the fluorescence optics and to discuss future steps needed to take full advantage of FDS in the analytical ultracentrifuge.

Use of FDS to Study Small Molecule-Protein Interactions

Example 1: Studying the interaction between rsEPCR and DPPC/E

Introduction:

The interaction between a soluble recombinant form of the endothelial protein C receptor (rsEPCR) and both activated and non-activated protein C have been previously characterized in our laboratory by analytical ultracentrifugation (AUC). In these studies it was shown that non-activated protein C and rsEPCR interact with a 1:1 stoichiometry and a $K_d = 2.0 \pm 0.9 \mu\text{M}$ ($n = 8$) in solution (unpublished, Kroe MSc 1998). The interaction between rsEPCR and activated protein C was shown to be slightly weaker with a $K_d = 6.0 \pm 0.6 \mu\text{M}$. Both interactions were shown to be calcium dependent with no further enhancement in binding with the addition of magnesium. The interaction between rsEPCR and thrombomodulin was also investigated and shown not to directly contribute to protein C binding.

EPCR shares a high level of homology with both the major histocompatibility complex (MHC) class 1 and cell differentiation (CD1) family of molecules. Both MHC class 1 and CD1 molecules function to present antigens, either peptide or lipid, to the immune system. The crystal structure of rsEPCR both bound to the gla-domain of protein C and in its unbound form have recently been solved (Oganesyan *et al.*, 2002). Interestingly, these structures revealed a bound

phospholipid present in the binding groove. This finding is consistent with the homology between EPCR and MHC class 1 and CD1 family molecules.

Oganesyan and co-workers have suggested that the interaction between protein C and EPCR is dependant on bound phospholipid and that the lipid:rsEPCR interaction is high affinity. Earlier work performed in Chuck Esmon's laboratory measured a $K_d = 30$ nM for the interaction between EPCR and activated protein C (Fukudome *et al.*, 1996). This value was achieved by a competitive binding flow cytometry assay that measures direct binding of activated protein C to the cell surface.

The apparent discrepancy between the solution centrifugation studies and the flow cytometry assay would suggest that the addition of lipid under the conditions of our solution studies may cause a large increase in binding affinity. While all of the materials used in our laboratory's AUC studies were obtained from the Esmon laboratory, samples were subjected to additional purification steps including gel filtration and dialysis. Oganesyan *et al.*, state that removal of phospholipid from the binding site could not be achieved by extensive washing steps although it is unclear how they are detecting the presence of bound lipid.

The goal of this work is to conduct a series of sedimentation velocity experiments using the absorbance optics and FDS to study the effect of both

phosphatidylethanolamine (DPPE) and phosphatidylcholine (DPPC) on the interaction between rsEPCR and protein C. This would include performing runs on each protein individually and then mixing them together in a 1:1 mole ratio in the presence and absence of either lipid. We hope to demonstrate the requirement for lipid to achieve the high affinity interaction measured on the surface and to rectify the apparent discrepancy between the solution and surface measurements.

Results:

A soluble recombinant form of the endothelial protein C receptor was received as a gift from Eli Lilly. Figure 12 shows the $c(S)$ distribution for 14 μM rsEPCR collected using the absorbance optics. These data fit to a S_{app} of 2.63 (2.61, 2.66) and a M_{app} of 31,524 (28,124; 43,224). In order to determine whether DPPC can bind to rsEPCR, FDS sedimentation velocity experiments were performed selectively following a synthetic DPPC labeled with nitrobenzoxadiazol (NBD) in the presence and absence of rsEPCR. The excitation and emission spectra of the NBD-DPPC were measured in buffer using an SLM-AB2 fluorimeter and revealed peaks at 453 nm and 544 nm respectively. The laser in the FDS optics emits light at a wavelength of 488 nm. In an ideal FDS experiment a fluorophore such as fluorescein, Oregon green or one of the Alexa dyes would be used. To compensate for being outside the optimum excitation range of the optics a relatively high concentration of fluorophore (400 nM) was used in the FDS experiments. It should be noted that in order to

detect this fluorophore using the absorbance optics a concentration of 100 μM NBD-DPPC would have to be used. No sedimentation was observed in a cell containing NBD-DPPC alone (data not shown). Figure 12 shows the $c(S)$ distribution for 10 μM rsEPCR in the presence of 400 nM NBD-DPPC as detected by the fluorescence optics. This data fit to a $S_{\text{app}} = 2.83$ (2.81, 2.85). These data show that NBD-DPPC binds to rsEPCR. The increase in sedimentation coefficient may indicate that a conformational change is occurring when NBD-DPPC binds to rsEPCR. However, it is also possible that the difference in sedimentation coefficient is the result in the temperature being un-calibrated in the FDS development system.

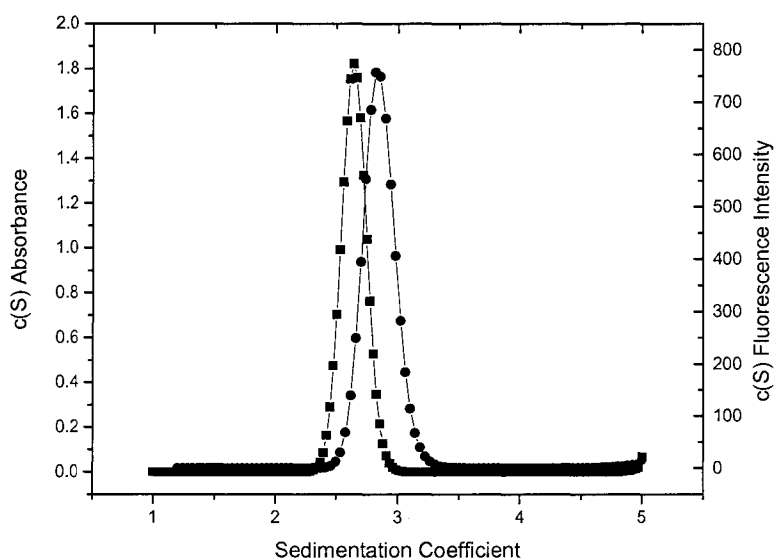


Figure 12: Sedimentation velocity of 14 μM rsEPCR (squares) collected with the absorbance optics and 10 μM rsEPCR + 400 nM NBD-DPPC (circles) collected with the fluorescence optics.

Discussion:

While this work is still in progress, these experiments demonstrate the application of FDS to study interactions between proteins and small molecules such as lipids and drugs. Selectively monitoring the lipid in the rsEPCR system will enable direct confirmation of whether the lipid is a necessary component of the high affinity rsEPCR/PC complex that otherwise would be difficult to determine. In addition, tracer sedimentation of fluorescently tagged lipids provides a means of studying lipid-protein interactions at concentrations below the lipid critical micelle concentration. This is an area of study previously inaccessible by AUC. The study of lipid-protein interactions by FDS-AUC will be valuable for the study of G-protein coupled receptors and other membrane bound proteins.

The next step in this series of experiments will be to sediment the rsEPCR/DPPC complex in the presence of protein C selectively following the sedimentation of the fluorescently tagged DPPC. Similar experiments will also be done using a fluorescein tagged DPPE. There is evidence in the literature for preference of DPPE over DPPC. Future work could also include a titration of rsEPCR at a constant concentration of lipid thus enabling a measurement of the binding affinity of DPPC/E for rsEPCR.

Use of FDS to Study High Affinity Interactions

Example 2: The interaction between GFP and anti-GFP

Introduction:

One of the long term goals of the non-ideality research discussed in Chapter 3 is to study the impact of high concentrations of background molecules of defined charge on protein-protein interactions. To take advantage of the FDS optical system and the use of GFP as a tracer molecule we choose to pursue the identification of a high affinity antibody to use as a model system.

Results:

A series of FDS sedimentation velocity experiments were performed with four different monoclonal anti-GFPs from various vendors. In each of these experiments the concentration of GFP was held constant while titrating the antibody over a range of concentrations. The first two monoclonal antibodies tested (Molecular probes and Zymed) did not appreciably bind to the GFP (data not shown). The conclusion from this result was that these antibodies most likely recognize internal epitopes that were unavailable for binding to the intact GFP. This conclusion is consistent with the fact that both antibodies are marketed for primary use in western blotting. The third antibody tested (BD-clonetechn) is marketed to work in both westerns and in immunocytochemistry. An interaction between the BD antibody and GFP was not detected (data not shown). This antibody apparently has a very low affinity. A fourth antibody

(MBL), marketed to work in immunoprecipitation applications, was shown to bind GFP in a 1:1 stoichiometry with high affinity (Figure 13).

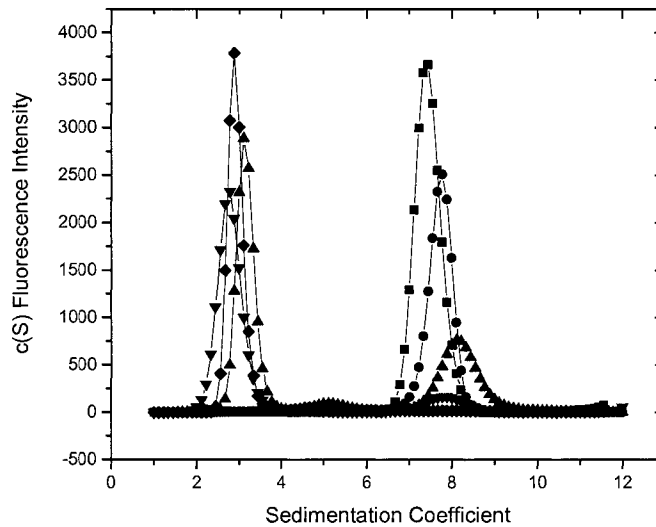


Figure 13: Sedimentation Velocity of 40 nM GFP titrated with 540 nM (squares), 60 nM (circles), 20 nM (up triangles), 7 nM (down triangles) and 0.3 nM (diamonds) anti-GFP (MBL).

The mass fractions of free GFP and the GFP:anti-GFP complex were determined by dividing the integrated areas of either the 2.6 S peak (GFP) or the 7.8 S peak (GFP:Anti-GFP) by the total area under the c(s) distribution curve. Plotting the mass fraction of the 7.8 S species and 2.6 S species as a function of antibody concentration (Figure 14), shows a crossover point occurring at approximately 20 nM, one-half of the total GFP concentration. This result is indicative of quantitative binding. The concentration of GFP must be

lowered in order to determine a binding constant for this interaction by sedimentation velocity.

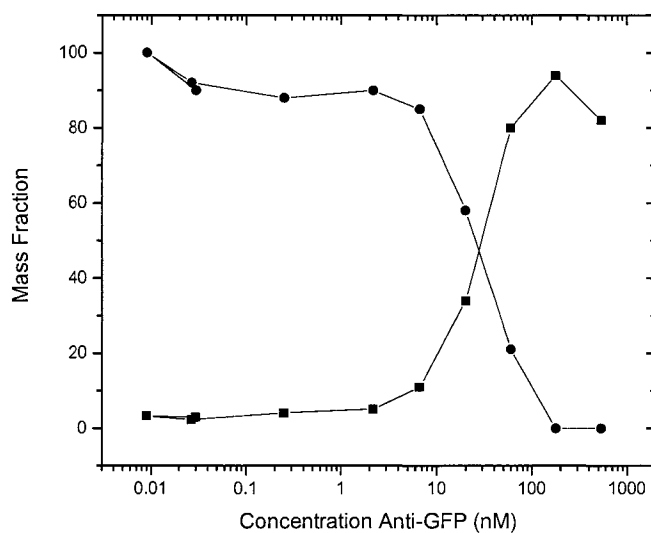


Figure 14: Mass Fraction of 7.8 S (squares) and 2.6 S (circles) species as a function of antibody concentration.

To further quantify the affinity of the GFP:anti-GFP interaction a fluorescence polarization experiment was conducted monitoring the depolarization of GFP as a function of antibody concentration (Figure 15). The K_d for this interaction is 1 nM.

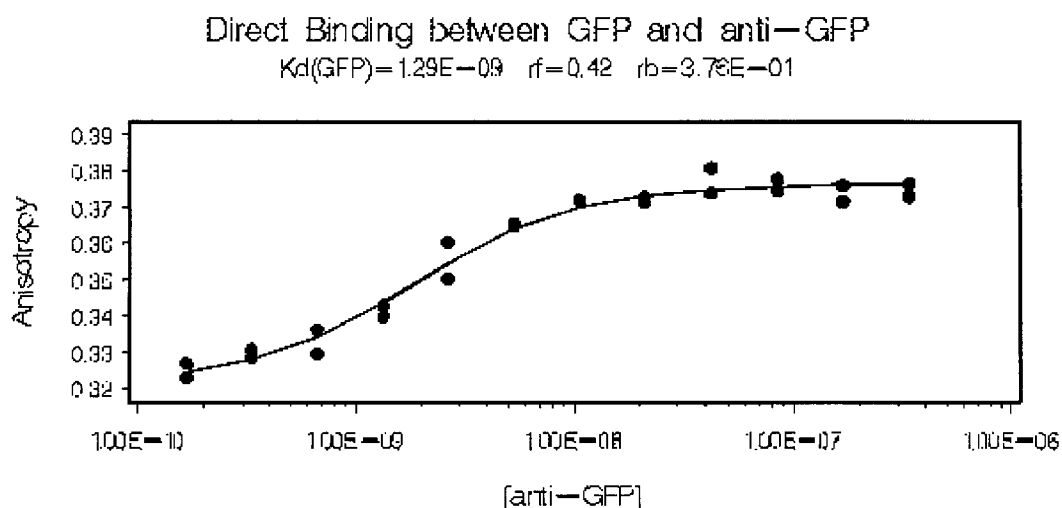


Figure 15: Direct binding of GFP to Anti-GFP as measured by fluorescence polarization.

Discussion:

One of the noted advantages of the FDS optics is the dynamic range of concentrations that can be examined. Specifically the ability to access low concentrations should enable high affinity equilibrium constants to be measured from centrifugation data. The K_d for the GFP-anti-GFP interaction was shown to be 1 nM as measured by fluorescence polarization. The K_d for this interaction could not be determined from the sedimentation velocity data due to quantitative binding. In order to measure a K_d in the range of 1 nM the concentration of the GFP would have to be lowered below 1 nM. At the time these experiments were conducted the power of the laser did not allow us to access the pM concentrations necessary to perform this type of analysis. The current FDS optics system has remedied this problem.

Another problem with this data set is that despite the concentration of GFP being held constant in each of the samples, the total fluorescence intensity varies from sample to sample. One potential explanation for the varying fluorescence intensity could be poor laser focus. It is also possible that the GFP is sticking to the windows or centerpieces causing differences in the total sedimenting signal. Problems with laser focus can be remedied; however the problem of fluorophores 'sticking' at low concentrations will always be a potential pit-fall. There are multiple ways to reduce or remove 'sticking' including adding small amounts of detergent or BSA. It is likely that the remedy will be unique for each system studied and therefore different additives should be attempted to optimize the buffer conditions when studying high affinity interactions at low protein concentration.

The goal of this work was to identify an interacting system that could be studied in concentrated solutions of defined charge. Choosing a system such as the GFP-anti-GFP interaction described here may not be ideal for these studies. A system with a more moderate affinity would provide better access to the study of the impact of the high concentration background solutions on the equilibrium constant. The next step in this work will likely be to identify another associating system for these studies.

Use of FDS to Study Sedimentation in Physiological Media

Use of the FDS optical system enables the investigation of the sedimentation behavior of tracer molecules in complex and concentrated solutions. An example of an application of this type was discussed in Chapter 3 where FDS was used to study the sedimentation of GFP in defined high concentration background solutions. One of the goals of the experiments in Chapter 3 is to bridge our understanding of the forces that are present in high concentration solutions and how those forces impact the biochemical constants that we measure in dilute solution relative to physiological conditions. In this section several examples are given highlighting the use of FDS to study the sedimentation of tracer molecules in biological media including human serum and *E. coli* lysates.

Example 3: Sedimentation Velocity of Alexa488-BSA in Serum and in Plasma

In this set of experiments, sedimentation of 100 nM Alexa488-Bovine Serum Albumin (Alexa488-BSA) was characterized in buffer, serum and in plasma (Figure 16). The sedimentation of the Alexa488-BSA is slowed from $S_{app} = 5.2$ (5.18, 5.21) in buffer to $S_{app} = 2.82$ (2.82, 2.83) in serum and $S_{app} = 2.84$ (2.83, 2.84) in plasma. All experiments conducted in serum and in plasma yielded identical results. For this reason only the data collected in serum will be discussed throughout the rest of this chapter.

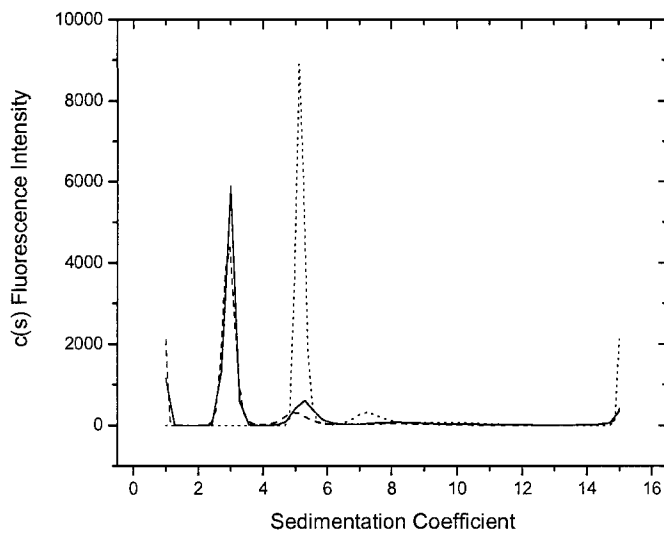


Figure 16: Sedimentation velocity of Alexa488-BSA in buffer (dotted line) Serum (solid line) and Plasma (dashed line).

The concentration of albumin (HSA) in human blood ranges from 34 - 54 mg/ml. Since BSA and HSA have similar masses it is likely that the Alexa488-BSA is co-sedimenting with HSA and therefore experiencing a significant amount of thermodynamic non-ideality as a result of both charge-charge repulsion and excluded volume. In addition to thermodynamic non-ideality there is likely a large degree of hydrodynamic non-ideality including the high viscosity and density of serum. Human serum has a viscosity that is eight times that of water (Altman, 1961). Serum contains a number of different macromolecules of varying masses ranging from small lipoproteins such as HDL to large macromolecules such as chylomicrons and antibodies. Both density and

viscosity gradients will be formed radially as each of these macromolecules sediments relative to its respective mass. These gradients complicate our ability to correct for the hydrodynamic forces that are occurring in the velocity cell. Further characterization will be needed to better understand sedimentation velocity data collected in serum.

Qualitatively it appears that the relative proportions of Alexa488-BSA monomer to dimer, assuming that the 5.2 S species in serum is dimer, are not affected in the crowded environment. If the dimer were in reversible equilibrium with the Alexa488-BSA monomer the amount of dimer might be expected to change due to the non-ideality expected in serum. Since there is no change it is likely that the dimer in the Alexa488-BSA sample is an incompetent byproduct of the purification.

Example 4: Sedimentation of Alexa488-IgG in Serum

The graph in Figure 17 shows the $c(s)$ fit for 500 nM Alexa488-IgG in buffer and for 100 nM Alexa488-IgG in human serum. The data fit to $S_{app} = 6.49$ (6.48, 6.52) and $S_{app} = 4.70$ (4.67, 4.75) respectively. The valence of IgG is predicted to be cationic, however, measured values in our laboratory have shown that the actual valences of IgGs are closer to neutral, at pH 7.4, than expected from calculations (Sue Chase, unpublished). The concentration of IgG in serum is estimated to be between 10-30 mg ml⁻¹ (Altman, 1961). As seen with the

Alexa488-BSA it is likely that the Alexa488-IgG is co-sedimenting with IgGs present in the serum. Since it is our prediction that the charge on these IgGs is close to neutral it is unlikely that a high degree of charge-charge is occurring with other serum components. Therefore, we would predict that the reduction in sedimentation coefficient of the Alexa488-IgG is primarily due to hydrodynamic non-ideality. This is supported by the observation that the percent reduction in sedimentation coefficient is less for Alexa488-IgG (30%) versus Alexa488-BSA (50%).

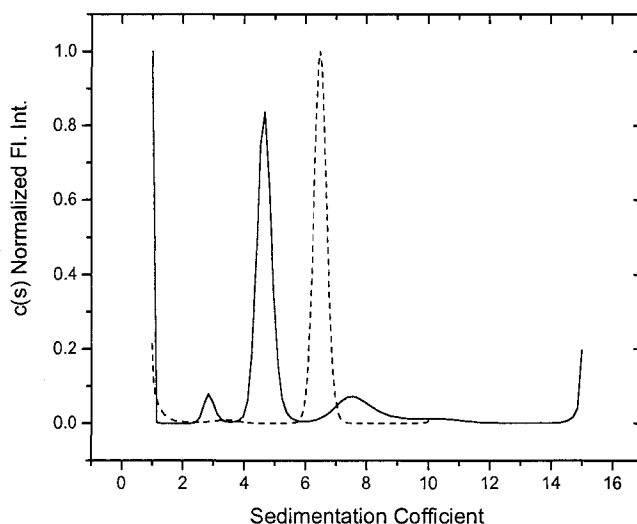


Figure 17: $c(s)$ fit for Alexa488-IgG in buffer (dotted line) and in serum (solid line).

A comparison of the $c(s)$ distribution for Alexa488-IgG in buffer versus serum shows the presence of several additional peaks when the Alexa488-IgG is spiked into serum. These two experiments were conducted six months apart so

it is possible that the small peak around 2.9 S is a degradation product. The larger peak around 7.5 S could be indicative of IgG dimerization either induced by the presence of serum or resulting from the age of the protein sample.

Example 5: Sedimentation of GFP in Human Serum

Figure 18 shows the raw data collected for 100 nM GFP in serum. The data show complex boundary patterns that are likely the result of both thermodynamic and hydrodynamic non-ideality. One interpretation of this type of boundary pattern could be that the GFP is showing a Johnston-Ogston (JO) effect (Johnston, (1946), Correia (1976)). JO effects occur when the sedimentation boundary of one component lowers the sedimentation in the presence of a second component. In this example, the sedimentation boundary of macromolecules present in serum that are larger than GFP will move more rapidly than the sedimentation boundary of the GFP. As a result the concentration of the GFP will be higher in the region behind the boundary of the faster sedimenting macromolecules and lower across the boundary of the faster macromolecules. It is not expected that the JO effect would be dependant on the concentration of the slower sedimenting component. However, a titration of GFP into serum from 544 nM to 4 nM shows that the JO type peak can be titrated (data not shown). Therefore it is likely that a second phenomenon is occurring. The nature of this phenomenon remains to be investigated.

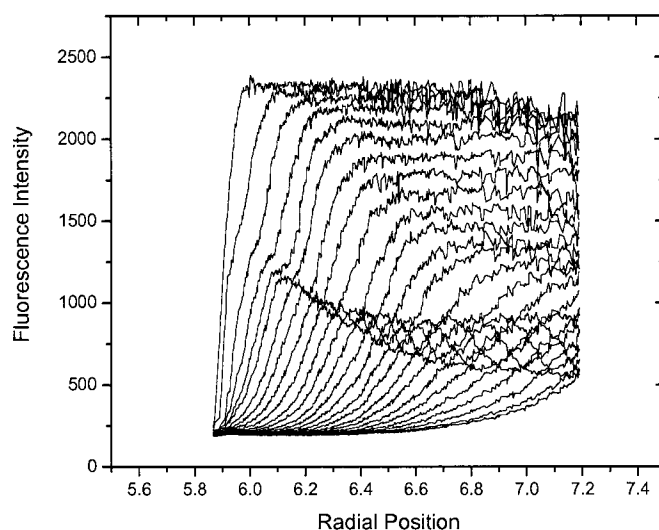


Figure 18: Raw sedimentation velocity data for 100 nM GFP in human serum.

Panel A of Figure 19 shows the raw data for 4 nM GFP in human serum, as mentioned above; there is no JO type peak at this concentration of GFP. The corresponding $c(s)$ fit to these data is shown in panel B of Figure 19. These data fit to a $S_{app} = 2.41$ (2.40, 2.41). The sedimentation coefficient for GFP in buffer is $S_{20,W} = 2.87$ (2.85, 2.89). Based on the total viscosity and density of serum the sedimentation coefficient of GFP would be expected to be significantly smaller than what is observed. These data suggest that the sedimentation of GFP may be coupled to other macromolecules of opposite charge as discussed in chapter 3. However, it is also likely that since GFP sediments more slowly than either HSA or IgG, its boundary is moving in a region of lower viscosity and density. The fact that GFP sediments more slowly than these high-concentration proteins also makes it subject to the JO effect. It

should be repeated; however, as discussed with the Alexa488-BSA and Alexa488-IgG data, viscosity and density gradients that occur in serum as a function of sedimentation complicate the interpretation of this result.

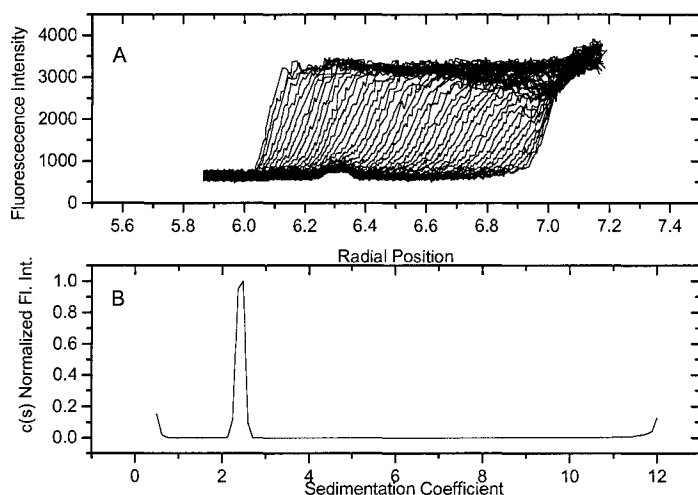


Figure 19: Raw sedimentation data of 4 nM GFP in serum (panel A) and the $c(s)$ fit to the data (panel B).

Example 6: Sedimentation of the GFP-anti-GFP Complex in Serum

In these experiments a 1:1 mixture of GFP and anti-GFP (MBL) was spiked into human serum at a concentration of 100 nM. The raw data for this experiment is shown in panel A of Figure 20. Interestingly, despite being at a concentration of 100 nM GFP, we do not see the same JO type peak in this data set as previously observed (Figure 18). The $c(s)$ fit to these data is shown in panel B of Figure 20. The peak at $S_{app} = 2.37$ (2.23, 2.38) is assumed to be free GFP based on the data for GFP alone in serum. The second peak at $S_{app} 4.22$ (4.21,

4.22) is assumed to be the 1:1 complex between GFP and anti-GFP. The K_d for this interaction is 1 nM (see example 2). The concentrations of GFP and anti-GFP are 100-fold greater than the K_d , therefore it would be expected that all of the GFP should be complexed with the anti-GFP under these conditions. These data suggest that the equilibrium constant for this interaction is shifted to a lower affinity in serum. This result is contrary to what would be expected based on the excluded volume of serum. These data suggest that the enthalpic environment of serum may be influencing the interaction between GFP and anti-GFP. It is also possible that hydrodynamic non-ideality is influencing this interaction. The next step in this work will be to perform a titration of the MBL anti-GFP to determine the K_d for this interaction in serum.

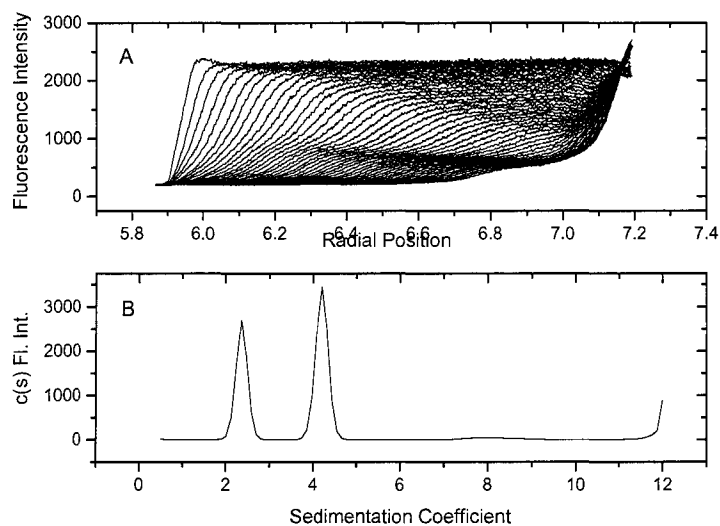


Figure 20: Raw sedimentation velocity data (panel A) and $c(s)$ fit for 100 nM GFP + 100 nM anti-GFP (panel B) in serum.

Example 7: Sedimentation Velocity of Fluorescein-DPPE in Serum

Figure 21 shows the raw data for 2 μ M fluorescein labeled DPPE sedimenting in human serum. These data show at least one sedimenting boundary, potentially a floating boundary and a JO type peak. The primary sedimenting boundary is likely fluorescein-DPPE bound to HSA. An estimate of the sedimentation coefficient for the primary sedimenting boundary can be calculated using equation 1:

$$s = \frac{\ln(r/r_m)}{w^2 t} \quad (1)$$

where r is the radial location of the midpoint of the sedimenting boundary, r_m is the meniscus position and $w^2 t$ is the angular velocity of the rotor. The apparent sedimentation coefficient for this boundary is 2 S. This is smaller than what we measured for Alexa488-BSA.

The floating boundary may be the result of the fluorescein-DPPE inserting into lipid micelles present in the serum. Further experimentation will be necessary to clearly identify all the phenomena occurring in these data. These data do show however, the potential for studying small molecule interactions in serum. One potential application could be for the study of HSA-drug interactions.

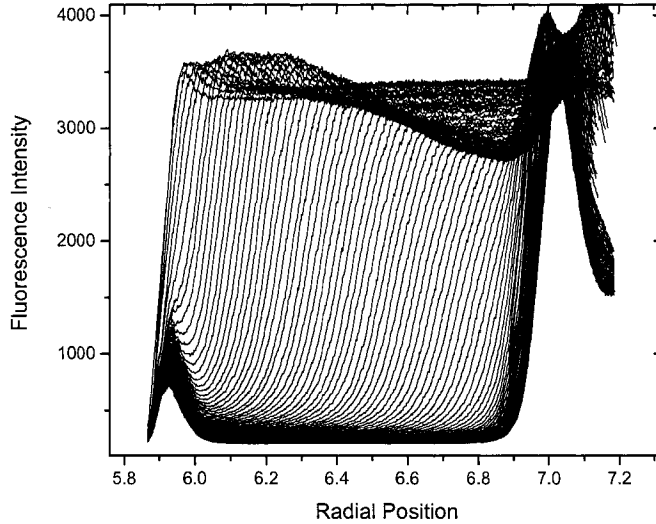


Figure 21: Raw sedimentation velocity data for 2 μ M fluorescein-DPPE in human serum.

Example 8: Sedimentation of GFP in *E. Coli* Lysates

Sedimentation velocity experiments were conducted adding a constant amount of GFP into a series of dilutions of *e.coli* lysate. The apparent sedimentation coefficient of GFP is increased in the presence of the lysate relative to buffer (Figure 22). These data do not take into account differences in viscosity and density that will further magnify the increase in sedimentation coefficient. The increase in sedimentation coefficient is dependent on the total concentration of protein in the *E. coli* lysate (data not shown). The sedimentation coefficient returns to the value measured in buffer as the concentration of lysate is decreased. These data suggest that the sedimentation of GFP is coupling to

other macromolecules in the lysate. Based on the observations discussed in Chapter 3 it is likely that GFP is selectively sedimenting with macromolecules of opposite charge present in the lysate.

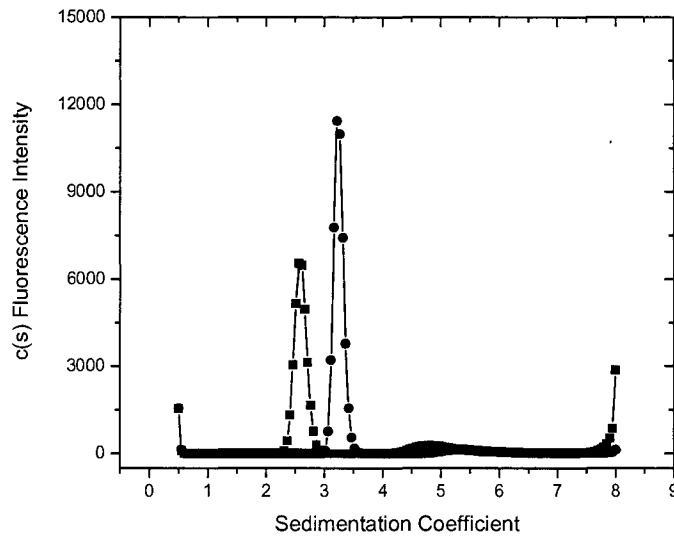


Figure 22: Sedimentation Velocity of 20 nM GFP in buffer (squares) and *E. Coli* Lysate (circles).

Summary

This chapter has highlighted several applications of FDS in the analytical ultracentrifuge. The application of FDS to answer biological questions is clearly still in its infancy. The examples presented here have demonstrated that FDS will enable the study of high affinity interactions in the AUC. With appropriate laser power and choice of fluorophore very low concentrations of

macromolecules can be detected. One of the remaining obstacles will be reducing sticking when working with low concentration applications. Many options exist for the treatment of sticking including the treatment of the cell components with chemicals such as silicone or through optimization of the buffer conditions. Time and experience will show which methods work the best.

This chapter has also highlighted several applications of tracer sedimentation using FDS in the AUC. These examples have shown that these types of experiments can yield very complicated boundary patterns. Much more data will need to be collected to better understand the forces that manifest these complicated boundary patterns. As our understanding of these forces builds more sophisticated fitting software will need to be developed to more completely capture all of the information in these data sets. In the meantime, qualitative data can be gathered from the systems that will be useful in testing basic theories and designing future experiments.

REFERENCES

Special Issue: EMBO Workshop on Biological Implications of Macromolecular Crowding, *Jour. Mol. Rec.* (2003), 17(5) 351-511.

D. Hall and A.P. Minton, Macromolecular crowding: qualitative and semi-quantitative successes, quantitative challenges, *Bioch. et Biophys. Act.* 1649 (2003) 127-139.

A.P. Minton, Confinement as a determinant of macromolecular structure and reactivity, *Biophys. Jour.* (1992) 63:1090-1100.

S.B. Zimmerman and A.P. Minton, Macromolecular crowding: biochemical, biophysical and physiological consequences, *Annu. Rev. Biophys. Biomol. Struct.* 22 (1993) 27-65.

A.P. Minton, The Influence of Macromolecular Crowding and Macromolecular Confinement on Biochemical Reactions in Physiological Media. *J. Biol. Chem.* 2001, 276(14) 10577-10580.

A.P. Minton, Molecular Crowding: Analysis of Effects of High Concentrations of Inert Cosolutes on Biochemical Equilibria and Rates in Terms of Volume Exclusion, *Meth. Enzym.* 295 (1998) 127-149.

R.J. Ellis, Macromolecular Crowding: obvious but underappreciated, *Trends in Biochem. Sci.*, 2001 26(10) 597-604.

B. v.d. Berg, R. J. Ellis and C. M. Dobson, Effects of macromoleuler crowding on protein folding and aggregation, *Eur. Mol. Bio. Org. Journ.* (1999), 18(24): 6927-6933.

G. Rivas and A.P. Minton, Tracer sedimentation equilibrium: a powerful tool for the quantitative characterization of macromolecular self and hetero-association in solution, *Bioch. Soc. Trans.* 2003 31(5) 1015-1019

P. Schuck, Size-distribution analysis of macromolecules by sedimentation velocity ultracentrifugation and lamm equation modeling. *Biophys J.* (2000) 78(3):1606-19

C. Tanford, *Physical Chemistry of Macromolecules*, New York, NY: Wiley, 1961.

C. K. Matthews and K. E. van Holde, *Biochemistry*, 2nd ed., Menlo Park, CA: Benjamin-Cummings Publishing Company, 1996.

MacGregor, I.K., Anderson, A.L., Laue, T.M., (2004) *Biophysical Chemistry* 108, 165-185.

Laue, T., (2004) *Drug Discovery Today: Technologies* (1)3:309-315.

Kroe, R. R. Master's Thesis, University of New Hampshire (1998).

Oganesyan V., Oganesyan, N., Terzyan, S., Qu, D., Dauter, Z., Esmon, N.L., and Esmon, C.T., (2002) *J. Biol. Chem.* **277**, 24851-4.

Fukudome, K., Kurosawa, S., Stearns-Kurosawa, D.J., He, X., Rezaie, A.R., and Esmon, C.T., (1996) *J. Biol. Chem.* **271**, 17491-8.

Johnston, J.P., Ogston, A.G., (1946) *Trans. Faraday Soc.* **42**, 789-799.

J.J. Correia, M.L. Johnson, G.H. Weiss, D.A. Yphantis, Numerical Study of the Johnston-Ogston Effect in Two-component Systems, *Biophys. Chem.* 1976, **5**:255-264.

P. L. Altman 1961, *Blood and other body fluids*, ASD Technical Report 61-199, Federation of American Societies for Experimental Biology, Washington, DC.

APPENDIX A

MEASUREMENT OF STOKES RADIUS

The Stokes radius for three of the proteins used in this work was measured by analytical ultracentrifugation. Measurement of the Stokes radius is necessary for calculation of the charge of a macromolecule from electrophoretic mobility data.

The Stokes radius can be calculated from the sedimentation coefficient of a macromolecule as measured in a sedimentation velocity experiment. The definition of the sedimentation coefficient is shown in equation 1:

$$s = \frac{M(1 - v\rho)}{Nf} \quad (1)$$

where M is the molecular weight of the macromolecule, v is the partial specific volume, ρ is the density of the solvent, N is Avogadro's number and f is the frictional coefficient. The frictional coefficient is defined in equation 2 as:

$$f = 6\pi\eta_0 R_s \quad (2)$$

where η_0 is the viscosity of the solvent and R_s is the Stokes radius of macromolecule. The Stokes radius can be calculated directly from the sedimentation coefficient if accurate values of M , v , ρ and η_0 are known.

Measurement of the effective reduced molecular weight, σ , by sedimentation

APPENDIX A continued

equilibrium alleviates the need to accurately determine the above listed parameters. The effective reduced molecular weight is defined in equation 3 as:

$$\sigma = \frac{M(1 - v\rho)\omega^2}{RT} \quad (3)$$

where M is the molecular weight, v is the partial specific volume, ρ is the density of the solvent, ω is the angular velocity of the rotor, R is the gas constant and T is the temperature. Dividing the sedimentation coefficient by the effective reduced molecular weight and rearranging results in equation 4:

$$R_s = \frac{\sigma RT}{s6\pi\eta_0\omega^2} \quad (4)$$

Calculation of R_s by this method only requires the additional measurement or calculation of solvent viscosity.

Sedimentation velocity experiments were conducted at 60,000 RPM and 20 °C in a pH 7.5 buffer containing 10 mM Tris, 100 mM KCl and 0.5 mM EDTA. The concentrations of GFP, Barstar and STI were 16 μ M, 29 μ M and 15 μ M respectively. Sedimentation was monitored by measuring the absorbance at 280 nm for each of the proteins. The non-interacting discrete species model in SEDFIT version 8.9 (available online at www.analyticalultracentrifugation.com) was used to fit each of the data sets (Schuck, 2000). Confidence intervals

APPENDIX A continued

(68.3%) on the sedimentation coefficient were calculated using the SEDFIT software. The values for the sedimentation coefficients are listed in table 2. Sedimentation equilibrium experiments were conducted in the same buffer listed above using 6-channel charcoal-epon centerpieces. Data was collected monitoring absorbance at 280 nm for Barstar and STI and at 485 nm for GFP at three protein concentrations at 15,000, 20,000 and 35,000 RPM at 20 °C. The data was analyzed using Winnonlin version 1.06 (available online at www.bbri.org/RASMB/rasmb.html) and the values for the fit effective reduced molecular weights are listed in table 2.

The Stokes radius was calculated from the sedimentation coefficient and effective reduced molecular weights using a calculated solvent viscosity obtained using the program SEDNTERP (available online at www.bbri.org/RASMB/rasmb.html) based on the buffer components.

	S	σ	$R_s \times 10^{-7}$
GFP	2.86 (2.84, 2.87)	0.86 (0.81, 0.92) RMS = 0.01	2.61 (2.48, 2.78)
Barstar	1.52 (1.51, 1.52)	0.34 (0.32, 0.36) RMS = 0.01	1.94 (1.84, 2.05)
Soybean Trypsin Inhibitor	2.16 (2.14, 2.19)	0.57 (0.54, 0.61) RMS = 0.01	2.29 (2.19, 2.42)

Table 2: Apparent sedimentation coefficients, effective reduced molecular weight and the calculated Stokes radius of GFP, Barstar and Soybean Trypsin inhibitor.

APPENDIX B

FDS OF GFP IN PEG, OVALBUMIN, RNASE A, HEL AND BARSTAR

The first experiment conducted to explore the role of charge in concentrated solutions was performed using 50 mg ml⁻¹ PEG, Ovalbumin and HEL (Figure 23). In this experiment lyophilized PEG, Ovalbumin and HEL were re-suspended in a pH 7.5 buffer containing 20 mM Tris, 100 mM KCl and 0.5 mM EDTA. A concentration of 10 nM GFP was added to each of the 50 mg ml⁻¹ background molecule stocks. Sedimentation velocity data was collected at 20 °C and 50,000 rpm using the FDS optics. The data were fit using the continuous $c(s)$ distribution model in Sedfit version 8.9.

In this experiment it was observed that while the sedimentation of GFP was slowed in the presence of PEG and Ovalbumin there was an apparent increase in sedimentation in the HEL solutions. This was the first piece of data alluding to the importance of charge in concentrated solutions.

APPENDIX B continued

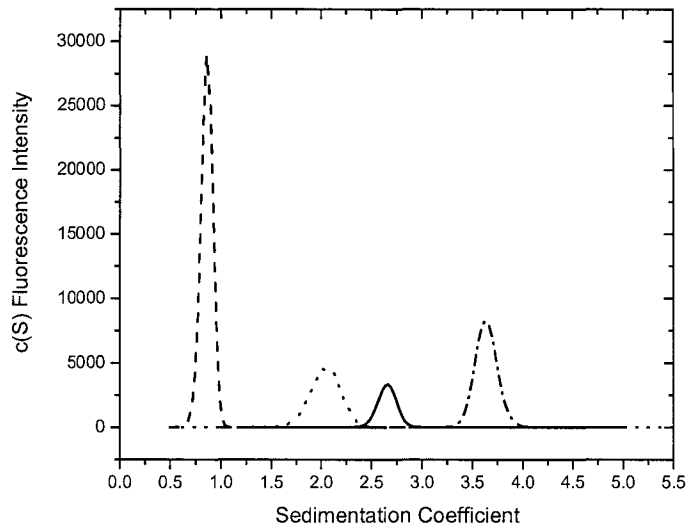


Figure 23: $c(s)$ distribution for 10 nM GFP in buffer (solid line), PEG (dashed line), Ovalbumin (dotted line) and HEL (dash-dot line)

After this initial observation several changes were made to the experimental design. As can be seen in Figure 23, PEG has a large effect on the sedimentation of GFP. This is most likely due to the high viscosity of the 50 mg ml^{-1} PEG solution. Therefore, the decision was made to replace PEG with Dextran, a spherical macromolecule whose viscosity increment is more closely matched to the charged protein background macromolecules. Additionally, Ovalbumin was replaced with STI to avoid potential JO effects that are likely to occur since the mass of Ovalbumin is greater than GFP. Switching to STI allows our tracer molecule to remain in a constant enthalpic bath over the

APPENDIX B continued

course of the velocity experiment. It should also be noted that for all subsequent FDS experiments in high concentration solutions the background molecules were exhaustively dialyzed against buffer prior to adding the tracer molecule.

Additional FDS velocity experiments were performed using proteins not discussed in Chapter 3. These proteins include Barstar (anionic) and RNase A (cationic). Barstar was chosen because it is small and relatively easy to express in large quantities. Unfortunately, the laser focus and quality of the data from the experiments where Barstar was used as the background molecule are quite poor (data not shown) and therefore need to be repeated. Experiments conducted using RNase A as the background molecule showed that RNase A can cause aggregation of GFP (data not shown). This is likely due to a bad batch of RNase A. These experiments should also be repeated.

The aggregation problem seen with the RNase A is also a reminder of the importance of choosing background molecules that are well characterized and are not prone to aggregation at high concentrations. Each of the background molecules used in the FDS experiments in Chapter 3 were characterized at high concentration using the interference optics as well as under dilute conditions using the absorbance optics (data not shown).

APPENDIX C

SOLUTION DENSITIES AND PARTIAL SPECIFIC VOLUME OF BACKGROUND MOLECULES

Solution density: The solution density of each of the concentrated background solutions was measured to enable conversion of apparent sedimentation coefficients to $S_{20,w}$ values. Density measurements were made on a Mettler/Par Precision Density Meter DMA O2D at 20°C in a buffer containing 10 mM Tris, pH 7.5, 100 mM KCl and 0.5 mM EDTA. The densitometer was equilibrated for at least one hour prior to taking measurements. An initial measurement of the density of air was recorded as the average of 15 readings followed by water, buffer, samples, water and then a final air reading. All samples were degassed prior to loading. The densitometer tube was equilibrated for a minimum of 10 minutes after loading before density readings were recorded. The tube was washed and dried with water and ethanol in between loading samples.

In order to determine the solution densities it is first necessary to calculate the apparatus constant for the densitometer using equation 1:

$$d_1 - d_2 = k(T_1^2 - T_2^2) \quad (1)$$

APPENDIX C continued

where d_1 is the density of water, d_2 is the density of air, T_1 is the period of oscillation measured for water and T_2 is the period of oscillation measured for air (1). To calculate the apparatus constant, T_1 and T_2 are calculated as the average of the oscillation readings taking at the beginning and end of the experiment and known values for the density of air and water under the experimental conditions are substituted for d_1 and d_2 . Once the apparatus constant has been determined the density of each of the samples can be calculated relative to the measured values for water.

Partial Specific Volume: The partial specific volume of a macromolecule is the effective volume per unit mass of a macromolecule dissolved in a solution. The apparent partial specific volume of a macromolecule can be determined experimentally by plotting solution density as a function of macromolecule concentration. The data are fit linearly and the slope of the line is used to calculate the partial specific volume using equation 2:

$$\bar{v} = \frac{1 - \text{slope}}{\rho_{s,c=0}} \quad (2)$$

where $\rho_{s,c=0}$ is the solvent density at zero macromolecule concentration.

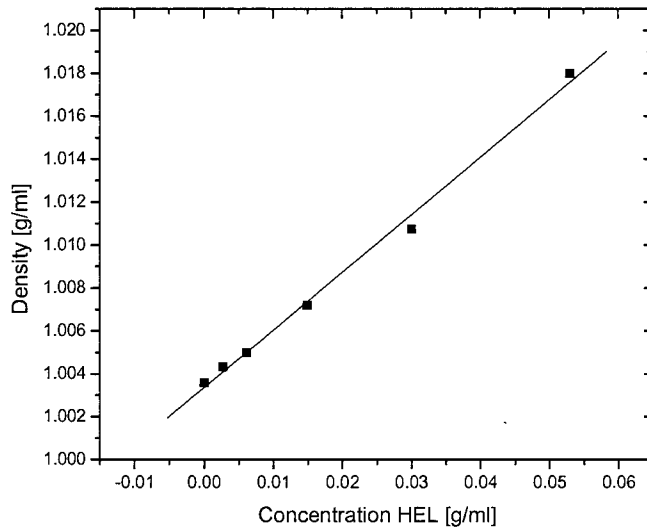
The results for HEL are shown in graph 24. The results for soybean trypsin inhibitor are shown in graph 25. The results for Dextran are shown in Graph 26. The results for Ovalbumin are shown in graph 27. The results for RNase A are shown in Graph 28.

APPENDIX C continued

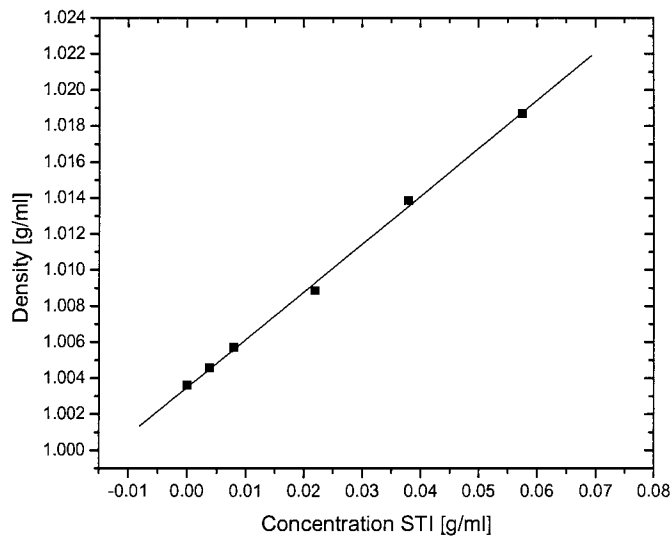
Table 3 shows the measured partial specific volumes for each of the macromolecules in addition to the equations to be used for calculating solution density as a function of macromolecule concentration. The difference between the measured values and values calculated using Sednterp (available online at www.bbri.org/RASMB/rasmb.html) varies between 0.41 % for Soybean Trypsin Inhibitor to 5.2 % for RNase A.

The larger discrepancies in the partial specific volume measurements may highlight inaccurate determination of the absolute protein concentration of these solutions. For the case of RNase A, multiple published values for the molar extinction coefficient were found. The value ultimately chosen for determination of concentration in this work may not accurately reflect the true composition of the commercially purchased RNase A. For the purposes of these studies accurate values for the partial specific volumes of the background molecules is not necessary for analysis. What are necessary are accurate measurements of density for each solution at a given concentration.

APPENDIX C continued

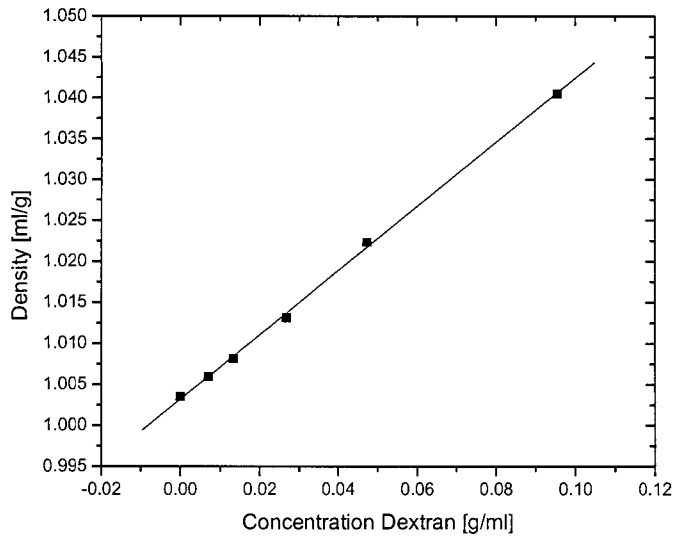


Graph 24: Solution density plotted as a function of HEL concentration.

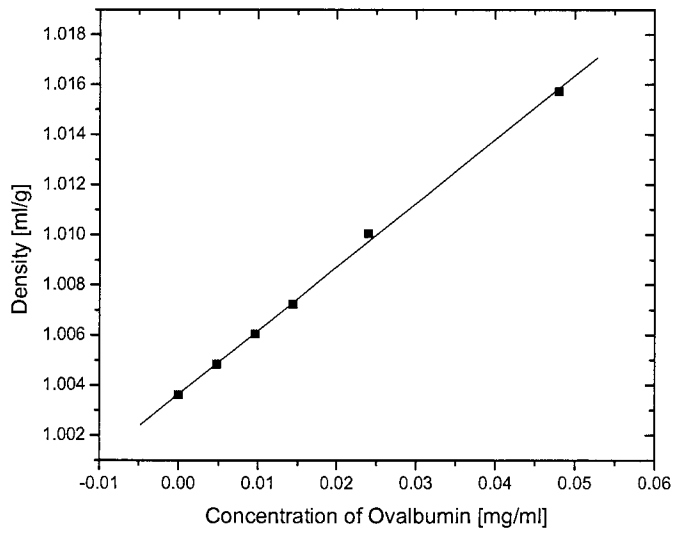


Graph 25: Solution density plotted as a function of STI concentration.

APPENDIX C continued

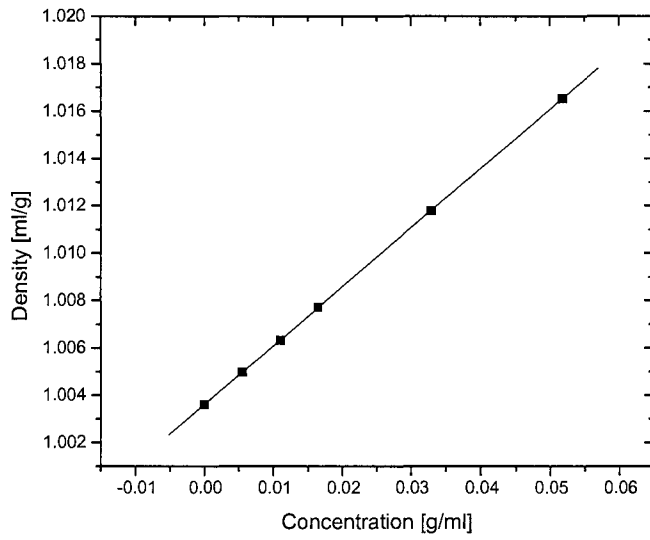


Graph 26: Solution density plotted as a function of Dextran concentration.



Graph 27: Solution density plotted as a function of Ovalbumin concentration.

APPENDIX C continued



Graph 28: Solution density plotted as a function of RNAse A concentration.

APPENDIX C continued

	Equation to Calculate Density as a Function of Concentration	Measured Partial Specific Volume [ml/g]	Calculated Partial Specific Volume [ml/g] (Sednterp)
Buffer	1.00362	n/a	n/a
HEL	$\rho = 1.00337 + 0.2680c$	0.726 ± 0.031	0.715
STI	$\rho = 1.00348 + 0.26562c$	0.731 ± 0.020	0.734
Dextran	$\rho = 1.00369 + 0.36921c$	0.629 ± 0.004	0.611
Ovalbumin	$\rho = 1.00364 + 0.25418c$	0.743 ± 0.003	0.737
RNAse A	$\rho = 1.00361 + 0.24920c$	0.748 ± 0.001	0.709

Table 3: Densities and Partial Specific Volumes of Background Molecules

1. Kratky, O., Leopold, H., Stabinger, H. The Determination of the Partial Specific Volume of Proteins by the Mechanical Oscillator Technique. *Methods in Enzymology*. 1973; 27:98-110.

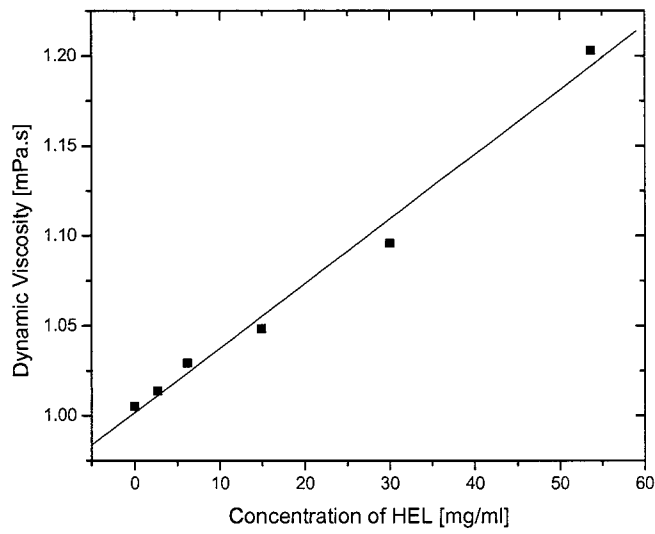
APPENDIX D

SOLUTION VISCOSITIES OF BACKGROUND MACROMOLECULES

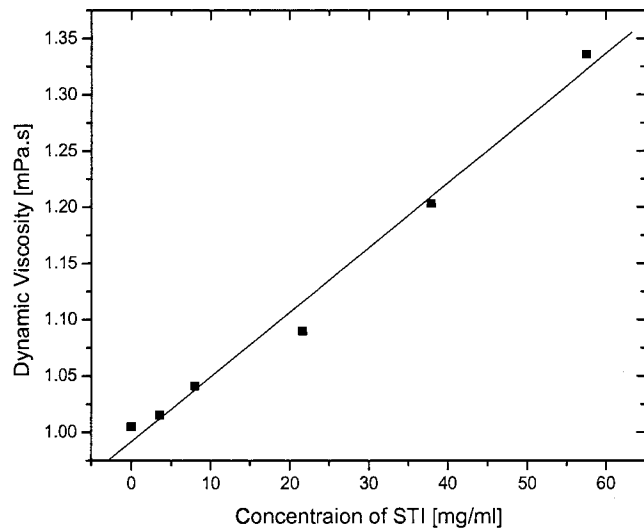
Solution viscosity: The solution viscosity of each of the concentrated background solutions was measured to enable conversion of apparent sedimentation coefficients to $S_{20,w}$ values. Viscosity measurements were made on an Anton Paar microviscometer. For each measurement 120 μl of the concentrated background molecule solution was loaded into the viscometer capillary tube. The corresponding measured density of the solution was entered into the software and dynamic viscosity measurements were made at 70° (n = 4), 60° (n = 4) and 50° (n = 6). Measured viscosities were plotted as a function of background molecule concentration and fit linearly to obtain an equation enabling calculation of the solution viscosity at any given concentration.

Graph 291 shows the viscosity data for the HEL solutions, Graph 30 shows the data for the STI solutions, Graph 31 shows the data for the Dextran Solutions, Graph 32 shows the data for the Ovalbumin solutions, and Graph 33 shows the data for the RNase A solutions. Table 4 contains the equations to be used for calculation of solution viscosity at any background macromolecule concentration.

APPENDIX D continued

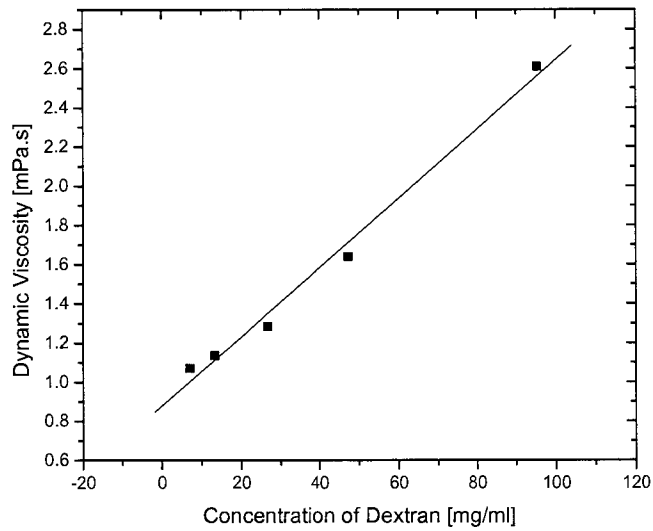


Graph 29: Solution viscosity plotted as a function of HEL concentration.

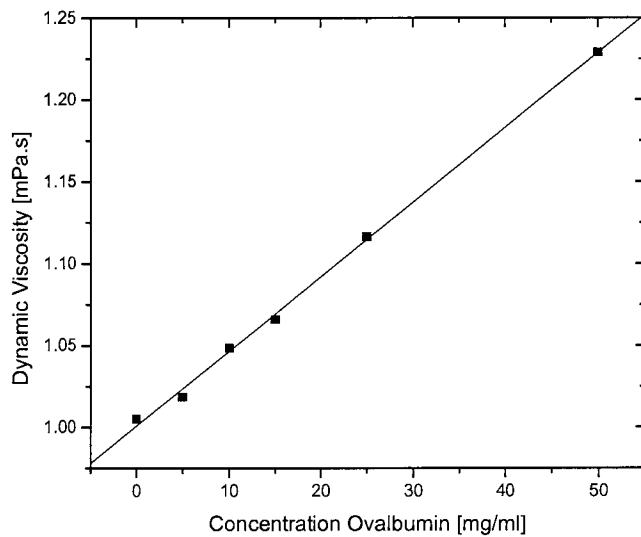


Graph 30: Solution viscosity plotted as function of STI concentration.

APPENDIX D continued

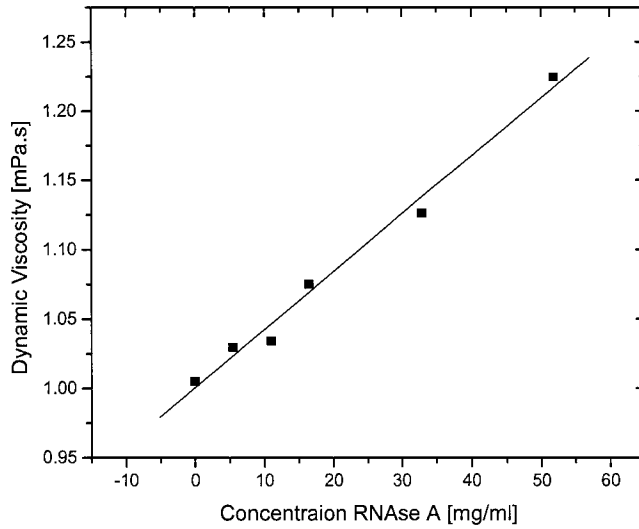


Graph 31: Solution viscosity plotted as a function of Dextran concentration.



Graph 32: Solution viscosity plotted as a function of Ovalbumin concentration

APPENDIX D continued



Graph 33: Solution viscosity plotted as a function of RNase A concentration

	Equation to Calculate Viscosity as a Function of Concentration
Buffer	1.0051
HEL	$\eta = 1.0016 + 0.00359c$
STI	$\eta = 0.9917 + 0.00575c$
Dextran	$\eta = 0.87705 + 0.01767c$
Ovalbumin	$\eta = 1.00078 + 0.00456c$
RNase A	$\eta = 1.00055 + 0.00418c$

Table 4: Equations for calculating density as a function of background macromolecule concentration.

APPENDIX E

ALEXA488-BSA IN VARIOUS HIGH CONCENTRATION BACKGROUNDS

In order to evaluate whether the phenomena described in Chapter 3 can be generally applied, a series of FDS sedimentation velocity experiments were conducted replacing GFP with Alexa488-BSA as the tracer molecule. In these experiments Dextran, Ovalbumin and HEL were used as background molecules at a concentration of 50 mg ml⁻¹. Sedimentation velocity data was collected using the FDS optics at 50,000 at 20 °C in a pH 7.5 buffer containing 10 mM Tris, 100 mM KCl and 0.5 mM EDTA. The data were fit using the continuous c(s) distribution model in Sedfit version 8.9.

Figure 34 shows the apparent sedimentation of Alexa488-BSA in Dextran, Ovalbumin, HEL and buffer. The apparent sedimentation of the Alexa488-BSA is slowed in the presence of Dextran and Ovalbumin relative to buffer. As with the GFP experiments the effect of Dextran and Ovalbumin appears to be primarily hydrodynamic. The apparent sedimentation of the Alexa488-BSA is increased in the presence of HEL. In addition to the increase in the apparent sedimentation coefficient of the Alexa488-BSA we also see the formation of larger complexes and possible aggregates in the HEL background. The nature

APPENDIX E continued

and composition of these larger species will require further experimentation. In the interim, these data support the conclusion that attractive non-specific charge-charge interactions occur in crowded solutions.

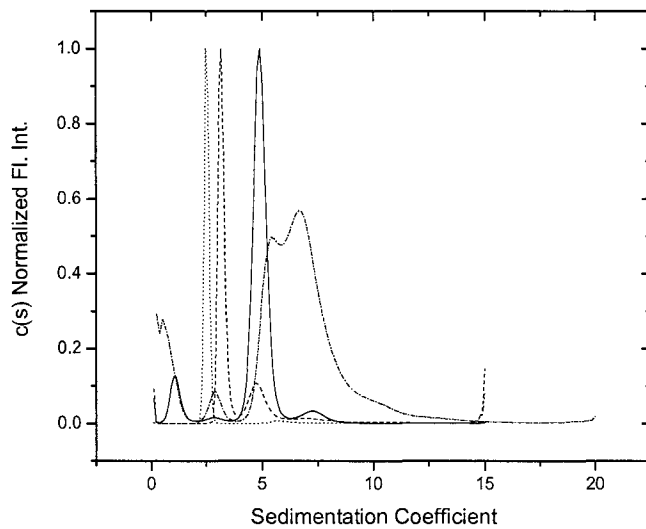


Figure 34: Sedimentation of Alexa488-BSA in buffer (solid black line), Dextran (dashed line), Ovalbumin (dotted line) and HEL (dash-dot line).